Available online at www.sciencedirect.com
ScienceDirect
Trans. Nonferrous Met. Soc. China 35(2025) 2462−2483
Transactions of Nonferrous Metals Society of China
www.tnmsc.cn

Improving creep-age forming ability of AA2219 alloy using asymmetrical rolling

Quan-qing ZENG[1], Dong-yao WANG[2], Bo-lin MA[1,3], Yong-qian XU[1,3], Ming-hui HUANG[1,2], Lei TANG[4], Chang-zhi LIU[5], Dong-yang YAN[5], Li-hua ZHAN[1,2,3], You-liang YANG[1,3]

1. Research Institute of Light Alloy, Central South University, Changsha 410083, China;
2. School of Mechanical and Electrical Engineering, Central South University, Changsha 410083, China;
3. State Key Laboratory of Precision Manufacturing for Extreme Service Performance, Central South University, Changsha 410083, China;
4. School of Materials Science and Engineering, Central South University, Changsha 410083, China;
5. Beijing Institute of Astronautical Systems Engineering, Beijing 100076, China;

Received 9 October 2023; accepted 6 August 2024

Abstract: The impacts of asymmetric rolling (ASR) and cold rolling (CR) on the creep-aging behavior of AA2219 alloys were revealed by creep deformation experiments, tensile tests, electron backscattered diffraction (EBSD) and transmission electron microscopy (TEM). The ASR specimens under creep stress condition of $1.2\sigma_{0.2}$ ($\sigma_{0.2}$ is the yield strength) displayed a 50% higher creep strain than the CR specimens. At a creep stress of $0.5\sigma_{0.2}$, the ASR specimens demonstrated remarkably mechanical properties, with a tensile strength of 525 MPa, a yield strength of 338 MPa, and an elongation of 15.2%. This enhancement can be ascribed to the effective grain refinement and promotion of recrystallization after ASR. Notably, ASR resulted in the formation of higher cube textures and a denser forest dislocation structure compared with CR. Additionally, ASR specimens demonstrated a higher density of dispersive, smaller θ' precipitates and larger average Taylor factors compared with CR specimens.

Key words: AA2219 alloy; asymmetric rolling; creep-aging behavior; texture; precipitate; mechanical properties

1 Introduction

Due to their exceptional mechanical properties, superior corrosion resistance, high electronic conductivity, and lightweight attributes, Al−Cu alloys have gained extensive application in the transportation and aerospace industries [1,2]. Recently, these alloys have exhibited significant potential for fabricating large-scale components for advanced aircraft and rockets [3,4]. Nonetheless, the limited creep strain capacity of Al−Cu alloys has notably constrained their utilization in producing large-sized components [5]. Although increasing the creep temperature is a common method to improve material creep response, it often comes at the expense of mechanical properties [6,7]. Hence, simultaneous enhancement of mechanical properties and creep deformation presents a critical challenge in contemporary research on creep-aging processes [8].

Since the previous century, creep-aging forming (CAF) has proven to be highly effective in fabricating large components with complex geometries, offering insights into the production of high-performance, large-sized components using Al−Cu alloys. The evolution of microstructure during creep aging process is recognized as closely

Corresponding author: Li-hua ZHAN, E-mail: yjs-cast@csu.edu.cn;
You-liang YANG, E-mail: yangyouliang@csu.edu.cn
https://doi.org/10.1016/S1003-6326(25)66827-0

connected to the processing conditions of the CAF [9,10]. Hence, many studies have focused on investigating how the forming parameters of the CAF impact the creep strain behavior and their effect on the microstructural evolution of Al alloys. The objective is to optimize the creep response and mechanical properties of components formed through creep-aging processes [1,11,12]. For instance, XU et al [13] illustrated that elevating the heating rate can weaken the strength of Al−Cu−Mg alloy. Additionally, CHEN et al [14] analyzed the creep-aging behavior of AA2219-T3 specimens under both tensile and compressive loading conditions across different stress levels. Their findings revealed a progressive reduction in the asymmetry of creep-aging behavior as stress levels increased. This phenomenon was attributed to variations in dislocation density and the distribution of precipitate sizes. To summarize, refining the CAF process has become a critical step in fabricating high-performance, complex components using Al alloys [15]. Although there has been considerable prior exploration into the creep deformation of Al alloys, achieving the enhanced creep deformation performance in Al−Cu alloys while preserving their exceptional mechanical properties remains a challenging goal.

The method of cold rolling, inducing substantial plastic deformation, has been recognized as an efficient means to produce materials with fine-grained or ultrafine-grained structures [16,17]. However, compared to conventional cold rolling (CR), asymmetric rolling (ASR) has demonstrated superior effectiveness in achieving plastic strains for a given thickness of rolled alloy sheets [18,19]. Considerable research efforts have been dedicated to examining the impact of ASR on the shear deformation [20,21], microstructural evolution [22,23], and mechanical properties [24,25] of rolled light alloy plates. Prior investigations [20,26] have validated that the ASR technique can effectively facilitate the artificial aging of Al alloy sheets, resulting in notable enhancements in mechanical properties compared to counterparts produced via conventional CR. Presently, the underlying reasons for the superior creep aging behavior of ASR samples have received limited exploration. Most studies have primarily focused on qualitative analysis of the strengthening behaviors of ASR samples, while the quantitative relationships among the microstructures, mechanical behaviors, and strengthening effects have remained unclear.

Therefore, in this study the creep-aging behavior and mechanical properties of asymmetrically rolled AA2219 alloy sheets were explored under different applied creep stresses. Additionally, a comprehensive characterization of microstructures, encompassing textures as well as the morphology and distribution of grains and precipitates, was undertaken to elucidate the relationships between applied creep stress and the resultant strengthening effects. These findings can provide valuable insights into optimizing the processing conditions for the combined ASR and CAF manufacturing approach. This optimization can facilitate the production of high-quality, large-sized, light-alloy components for aerospace exploration.

2 Experimental

2.1 Asymmetric cold rolling

In this study, AA2219 Al−Cu alloy hot-rolled plates obtained from Southwest Aluminum (Group) Co., Ltd., China, with a thickness of approximately 5 mm, were employed. The nominal chemical composition of the AA2219 alloy is shown in Table 1. Before cold rolling, a plate measuring 200 mm × 100 mm × 5 mm was cut from the initial hot-rolled alloy sheet and underwent annealing at 515 °C for 1 h, followed by water quenching. The cold rolling mill had a diameter of 100 mm. For the CR specimens, the rotation speed of the upper roller remained constant at 15 r/min, while the asymmetric ratio (ω_1/ω_2) of the lower roller could be adjusted by varying its rotation speed. In this investigation, the ω_1/ω_2 value was set at 1.8, denoted as ASR. All specimens underwent cold rolling to a thickness of 2.5 mm via six consecutive rolling passes at room temperature, resulting in a thickness reduction ratio of 50%. Following this, the specimens were subjected to solution treatment

Table 1 Nominal chemical composition of 2219 Al−Cu alloy (wt.%)

Cu	Mg	Mn	Si	Fe
5.8−6.8	0.02	0.2−0.4	0.09	0.13

Zn	Zr	Ti	Al
0.1	0.1−0.25	0.07	Bal.

in a resistance furnace at 515 °C for 1 h, followed by water quenching. Before creep-aging, all specimens were in the T4 state.

2.2 Creep-aging and mechanical properties tests

Initially, uniaxial tensile tests were conducted on both CR and ASR specimens after solution treatment using an MTS-Model E45 testing machine to assess their average yield strength ($\sigma_{0.2}$) at 165 °C. The measured average values of $\sigma_{0.2}$ were 171.2 MPa for the CR specimens and 157.3 MPa for the ASR specimens. Following the tensile tests, creep-aging test was conducted using a SUST-D5 creep testing machine equipped with a resistance furnace. Two groups of specimens were creep-aged at 165 °C for 16 h under various applied stress levels, namely $0.5\sigma_{0.2}$, $0.7\sigma_{0.2}$, $0.9\sigma_{0.2}$, $1.0\sigma_{0.2}$, and $1.2\sigma_{0.2}$, respectively. Furthermore, errors in temperature and stress during the creep-aging deformation tests were carefully controlled within a range of ±3 °C and ±2 MPa to ensure the reliability of experimental data. Subsequently, the tensile mechanical properties of the specimens after creep-aging deformation were also evaluated at a constant engineering strain rate of 1×10^{-3} s^{-1}. Three identical specimens were tested for each set of processing conditions described above.

2.3 Microstructure characterization

The surfaces of all specimens were initially ground using abrasive papers, followed by fine polishing with 3 μm diamond grinding paste and 50 nm colloidal silica suspension to eliminate the strained layers induced by prior mechanical grinding. Subsequently, the polished specimens were cleaned using ethanol to remove any residual silica particles. Following the cleaning process, the microstructure of every sample processed under various conditions was methodically analyzed using an FEI Helios 5 CX scanning electron microscope (SEM) outfitted with an electron backscattered diffraction (EBSD) detector. The OIM software was employed to identify the distinctive textures in the two specimens. The proportion of each texture was calculated with an angular tolerance of 20°. To examine the shape and size distribution of precipitates within the Al−Cu matrix, thin foils measuring 3 mm in diameter were extracted from the creep-aged specimens and polished to approximately 80 μm in thickness. Subsequently, these thin foils underwent twin-jet electropolished in an electrolyte comprising approximately 30 vol.% nitric acid and 75 vol.% methanol, applying a voltage of 16 V at −25 °C. Ultimately, transmission electron microscopy (TEM) analysis was conducted on these thin foils using a Talos F200X microscope operating at 200 kV. In order to mitigate statistical discrepancies, the thickness of each sample was measured at a minimum of three θ' phases, and the average of five measurements was considered as the indicative thickness value.

3 Results

3.1 Microstructure after solution treatment

Figure 1 displays optical microscope (OM) images of distinct layers subjected to diverse rolling processes followed by subsequent heat treatment. Interestingly, both the ASR and CR specimens presented a predominantly equiaxed grain structure. Notably, the ASR samples exhibited a greater prevalence of fine grains surrounding the coarse grains, suggestive of prominent shear bands induced during the asynchronous rolling process. Conversely, the CR samples also manifested some fine grains, although their amount was notably less in comparison to the ASR samples. Moreover, the disparity in grain size within each layer was smaller in the ASR samples, and a similar trend was observed in the CR samples as well.

The grain size and misorientation angle distributions of different layers in the two rolled specimens are depicted in Figs. 2(a−c) and Figs. 3(a−c), respectively. The white lines represent the low-angle grain boundaries (LAGBs) with misorientation angles ranging from 2° to 15°, while black lines indicate high-angle grain boundaries (HAGBs) with misorientation angles >15°. The average grain size in the three layers of the ASR specimen appears remarkably similar, ranging from 12.6 to 14.8 μm (Figs. 2(a−c)). Hence, given the utilization of thin plates in this study, the strain gradient induced by the ASR might be negligible, exerting minimal influence on the subsequent recrystallization process. Moreover, regarding the CR specimens, the average grain size demonstrated a relatively consistent response to the position along the thickness, ranging from 17.6 to 20.7 μm across various layers (Figs. 3(a−c)). Crucially, in each position, the average grain size in the ASR specimen

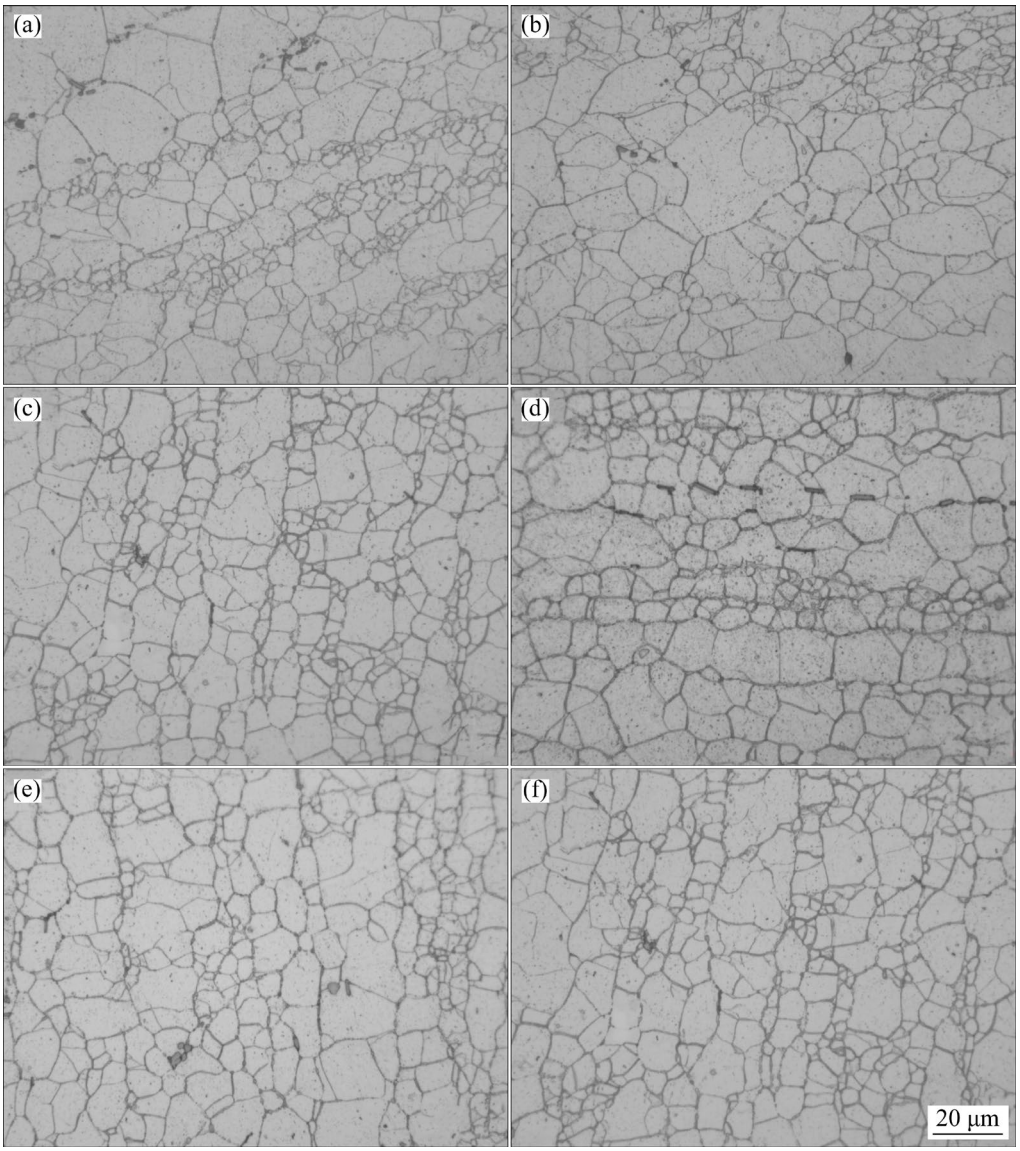

Fig. 1 OM images of CR and ASR samples: (a) Top layer, ASR; (b) Top layer, CR; (c) Middle layer, ASR; (d) Middle layer, CR; (e) Bottom layer, ASR; (f) Bottom layer, CR

consistently showed smaller values compared to its CR counterpart.

The grain size and misorientation angle distributions of each layer in the two rolled specimens are depicted in Figs. 2 and 3, respectively. The white lines represent LAGBs with misorientation angles ranging from 2° to 15°, while black lines indicate HAGBs with misorientation angles >15°. The average grain size in the three layers of the ASR specimen appears remarkably similar, ranging from 12.6 to 14.8 μm (Figs. 2(a−c)). Hence, given the utilization of thin plates in this study, the strain gradient induced by the ASR might be negligible, exerting minimal influence on the subsequent recrystallization process. Moreover, regarding the CR specimens, the average grain size demonstrated a relatively consistent response to the position along the thickness, ranging from 17.6 to 20.7 μm across various layers (Figs. 3(a−c)). Crucially, in each position, the average grain size in the ASR specimens consistently showed smaller values compared to its CR counterpart.

Table 2 displays the fractions of HAGBs and LAGBs in the CR and ASR specimens. Remarkably, the ASR specimens exhibited a higher proportion of HAGBs compared to the CR specimen. Additionally, the recrystallization fraction in the ASR specimens was notably enhanced, especially in the mid-layer. Conversely, the HAGBs fraction in the mid-layer of the CR specimens was only 46.8%,

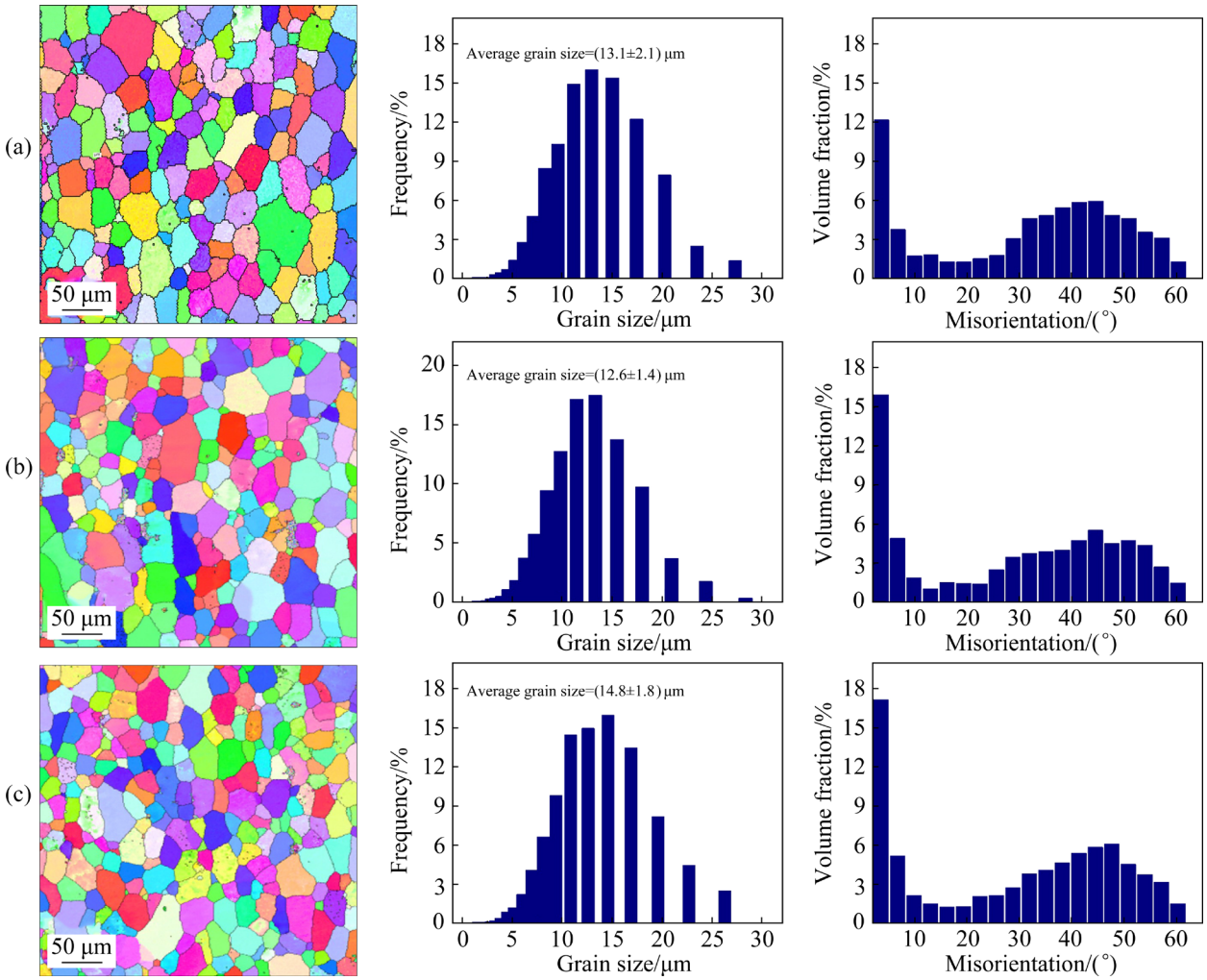

Fig. 2 IPF maps and corresponding distributions of grain size and misorientation angle at different layers of ASR specimen after solid solution: (a) Top layer; (b) Middle layer; (c) Bottom layer

which was significantly lower than that of the ASR mid-layer (72.1%). Notably, substantial differences in recrystallized grain structure were observed between the bottom and top of the ASR specimens compared to those of the CR specimens. This suggests that ASR effectively enhances the degree of recrystallization. The differences in grain size between the ASR and CR specimens, as evident from Table 2, could be attributed to the presence of shear banding-induced grain structure kinks in the ASR specimen, resulting in distinct grain sizes during the solution treatment [27].

An analysis of the orientation distribution function (ODF) was conducted on the top, middle (center), and bottom sections to investigate the texture variation (Fig. 4). ODFs were generated for Φ_2 angles of 0°, 45°, and 65°. Considering the composition of the Al alloy post-rolling, typical S $(123)\langle 63\bar{4}\rangle$, Copper $(112)\langle 11\bar{1}\rangle$, and Brass $(110)\langle \bar{1}12\rangle$ components were identified [28]. Cube $(001)\langle 100\rangle$ and Goss $(110)\langle 001\rangle$ textures were identified, arising from a solid solution. Interestingly, the ASR specimens, following the solution treatment, did not present shear texture components with orientations $\{111\}\langle 110\rangle$ and $\{100\}\langle 110\rangle$. Therefore, the shear texture component was disregarded in the present study. In summary, both specimens displayed typical recrystallization textures despite with varying intensity after the solution treatment.

Figures 5(a_1−a_3, b_1−b_3) depict the distributions of crystal orientation for the two specimens after solution treatment. Figure 5(c) outlines variations in the proportion of texture components between the CR and ASR specimens. Notably, the primary textures in both specimens consist of Goss, Brass,

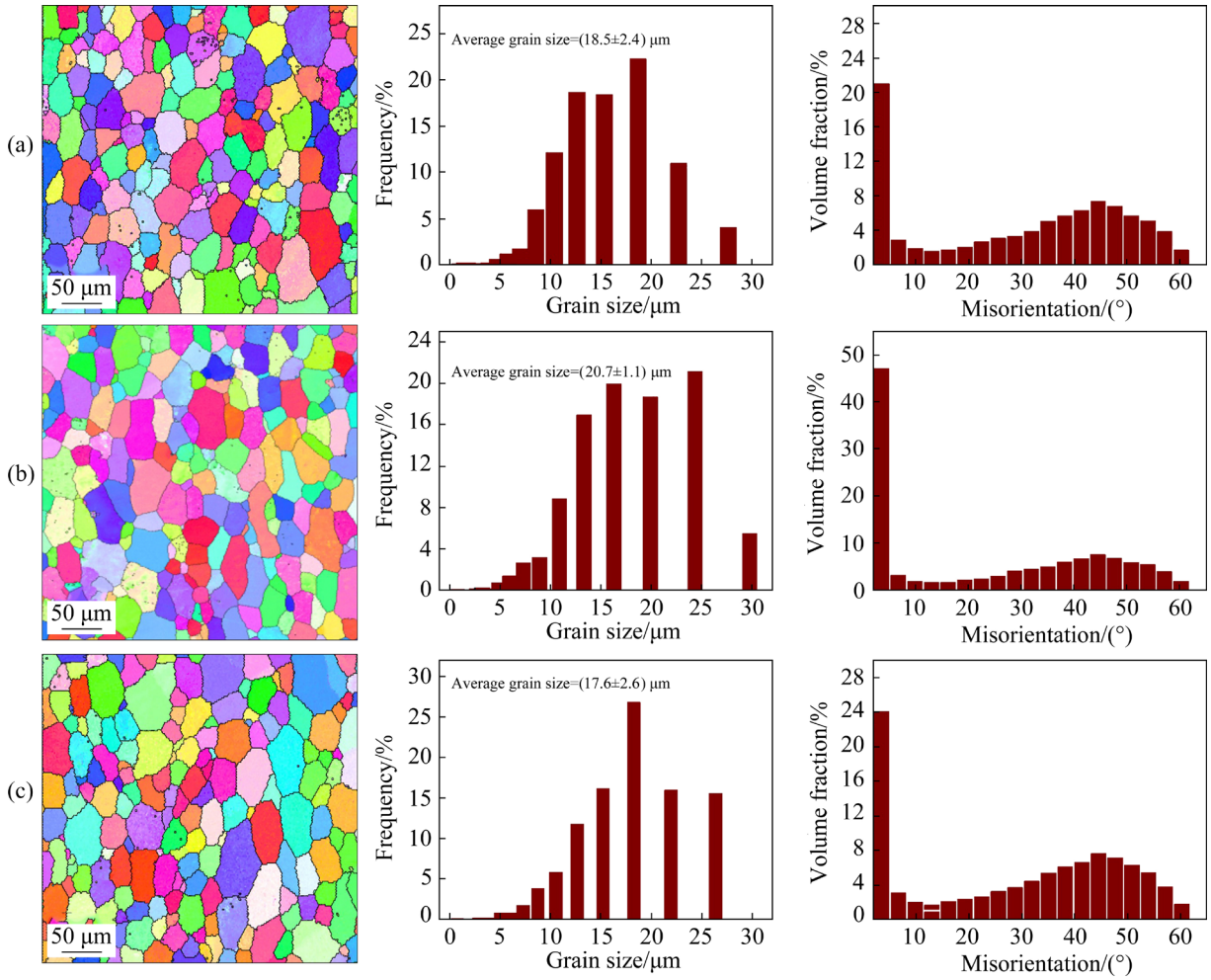

Fig. 3 IPF maps and corresponding distributions of grain size and misorientation angle at different layers of CR specimen after solid solution: (a) Top layer; (b) Middle layer; (c) Bottom layer

Table 2 Distributions of misorientation angles and average grain size of ASR and CR specimens after solid solution

Specimen	Layer	Fraction/%		Grain size/μm
		HAGBs	LAGBs	
ASR	Top	76.5	23.4	13.1±2.1
	Middle	72.1	29.8	12.6±1.4
	Bottom	75.6	24.3	14.8±1.8
CR	Top	69.4	30.5	18.5±2.4
	Middle	46.8	53.2	20.7±1.1
	Bottom	67.7	32.2	17.6±2.6

Cube, and Copper textures. Moreover, nearly equivalent amounts of Brass textures were detected within the layers of both CR and ASR specimens. The ASR specimens exhibited elevated levels of Cube, S and Goss textures across the upper layer, middle layer, and bottom layer. In contrast to the CR specimens, the ASR counterparts demonstrated a greater prevalence of Cube textures in the solid state, along with an increase of S textures. On the other hand, the CR specimens were primarily distinguished by Goss and Copper textures in the solid solution state. Additionally, the CR specimens exhibited a greater proportion of Goss textures in every layer when compared with the ASR specimens. Remarkably, recrystallized textures (cube) emerged as the predominant texture types in the ASR samples, whereas copper textures constituted the primary texture components in the CR specimens.

3.2 Creep-aging behavior

The yield strengths recorded for the ASR and CR specimens at 160 °C were 171.2 and 157.3 MPa, respectively. These findings were utilized to ascertain the applied creep stresses for both ASR

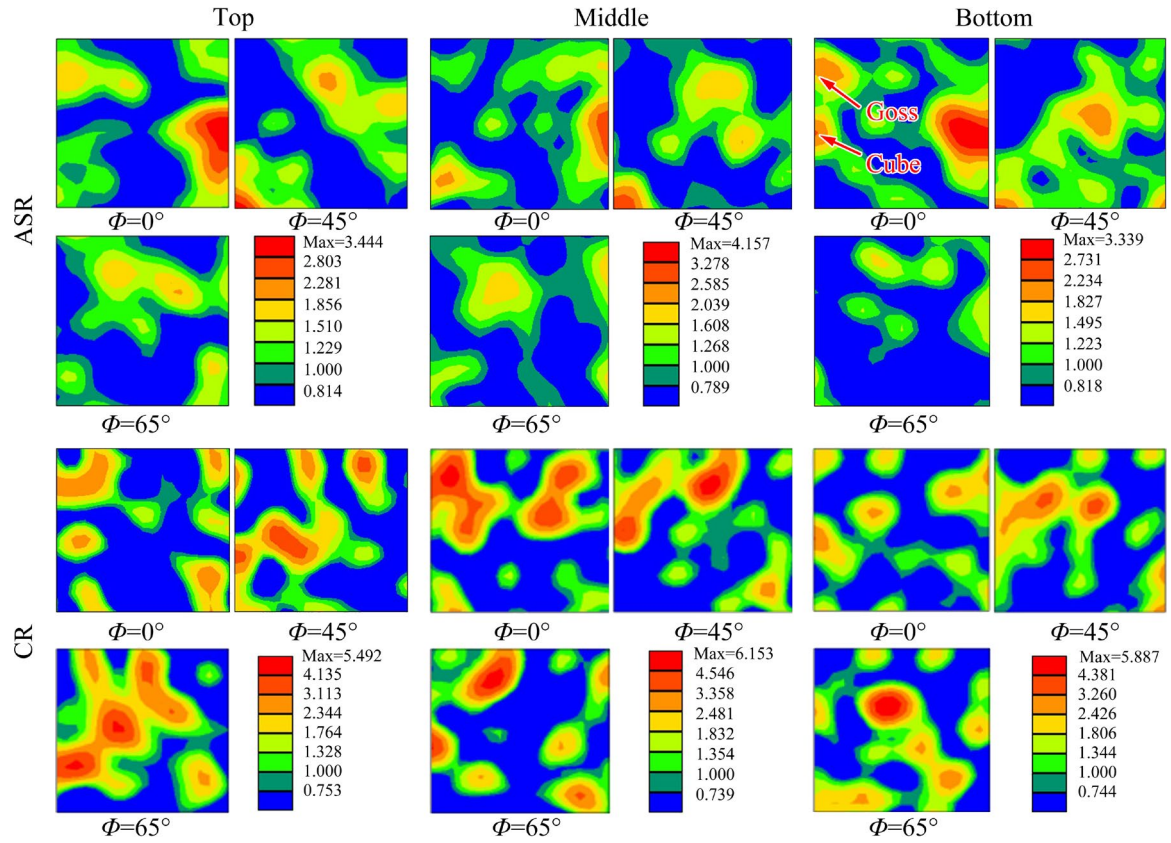

Fig. 4 ODF figures of different specimens

and CR specimens, determined as $0.5\sigma_{0.2}$, $0.7\sigma_{0.2}$, $0.9\sigma_{0.2}$, $1.0\sigma_{0.2}$, and $1.2\sigma_{0.2}$. Figure 6 illustrates the creep-aging curves and creep strain rates of the ASR and CR specimens under various initial applied stresses at 165 °C. As shown in Fig. 6, both CR and ASR specimens display similar traits. The creep-aging curves consist of an initial primary creep stage succeeded by a steady-state creep stage, typical of conventional creep-aging behavior [29]. In the primary stage, there is a rapid increase in the creep strain, accompanied by relatively high creep strain rates [5].

After a creep-aging period of 16 h under a high creep stress of $1.2\sigma_{0.2}$, the ASR specimens displayed a creep strain value of 1.91%, whereas the CR specimens demonstrated a value of 2.86%. Conversely, under the same high creep stress of $1.2\sigma_{0.2}$, the creep strain rates were 0.21 s^{-1} for CR and 3.7 s^{-1} for ASR following a creep-aging period of 16 h. Under creep stress of $0.7\sigma_{0.2}$, the ASR specimens recorded creep strain values of 0.364%, whereas the CR specimens exhibited values of 0.287%. Correspondingly, the creep strain rates were 0.823 s^{-1} for ASR and 0.746 s^{-1} for CR. These findings suggested that the ASR displayed greater total creep deformation than CR under varied stress conditions despite both exhibiting a similar trend in creep deformation rates.

Supplementary creep tests were conducted to explore the influence of creep strain under different stress levels. The ASR specimens consistently exhibited the highest steady-state creep rate in comparison to the CR specimens across a range of stress conditions. The correlation between the steady-state creep strain rate ($\dot{\varepsilon}$) and the applied creep stress (σ) can be expressed as follows [8]:

$$\dot{\varepsilon}=A\sigma^{n} \tag{1}$$

By taking the logarithm of both sides of Eq. (1), we can determine the material constant (A) and stress exponent (n) as follows [30]:

$$\ln \dot{\varepsilon}=\ln A+n\ln \sigma \tag{2}$$

The stress exponent, an important factor indicating the deformation mechanism in creep behavior, was calculated using Eqs. (1) and (2). A stress exponent value falling between 1 and 2 implies a creep mechanism controlled by diffusion, whereas a value exceeding 4 indicates creep mechanism controlled by dislocation [14]. Plotting

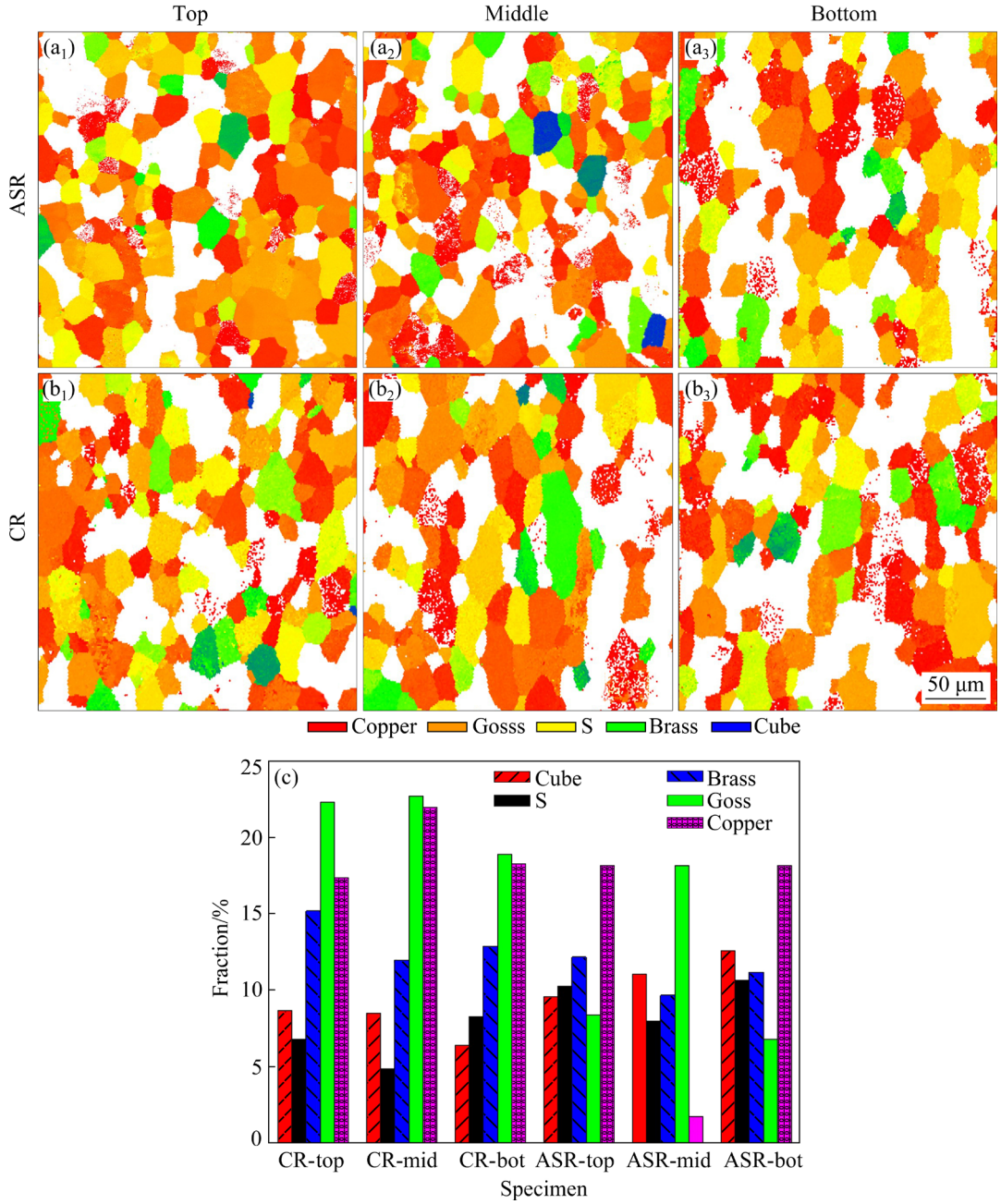

Fig. 5 Crystal orientation distribution diagrams of specimens after solution treatment: (a_1−a_3) ASR; (b_1−b_3) CR; (c) Distribution of main textures in ASR and CR specimens

the relationship between $\ln\dot{\varepsilon}$ and $\ln\sigma$ using Eqs. (1) and (2), the stress exponent n was determined, as illustrated in Fig. 7. By employing linear regression analysis, the stress exponents were found to be 1.72 and 2.38 for ASR and CR specimens at creep stresses below $1.0\sigma_{0.2}$, respectively. However, when the creep stresses surpassed $1.0\sigma_{0.2}$, the stress exponents for the ASR and CR specimens were determined to be 6.82 and 7.67, respectively. Consequently, it suggests that a dislocation creep mechanism governs the high creep stress range, whereas the low creep stress range adheres to a diffusion creep mechanism.

3.3 Mechanical properties

Figure 8 displays the stress−strain curves at room temperature for CR and ASR samples under various stress levels of $0.5\sigma_{0.2}$, $0.7\sigma_{0.2}$, $0.9\sigma_{0.2}$, $1.0\sigma_{0.2}$, and $1.2\sigma_{0.2}$. In comparison to the CR specimens, the ASR specimens showed higher ultimate tensile strength (UTS) and yield strength (YS) at similar stress levels. Additionally, the elongation (EL) of

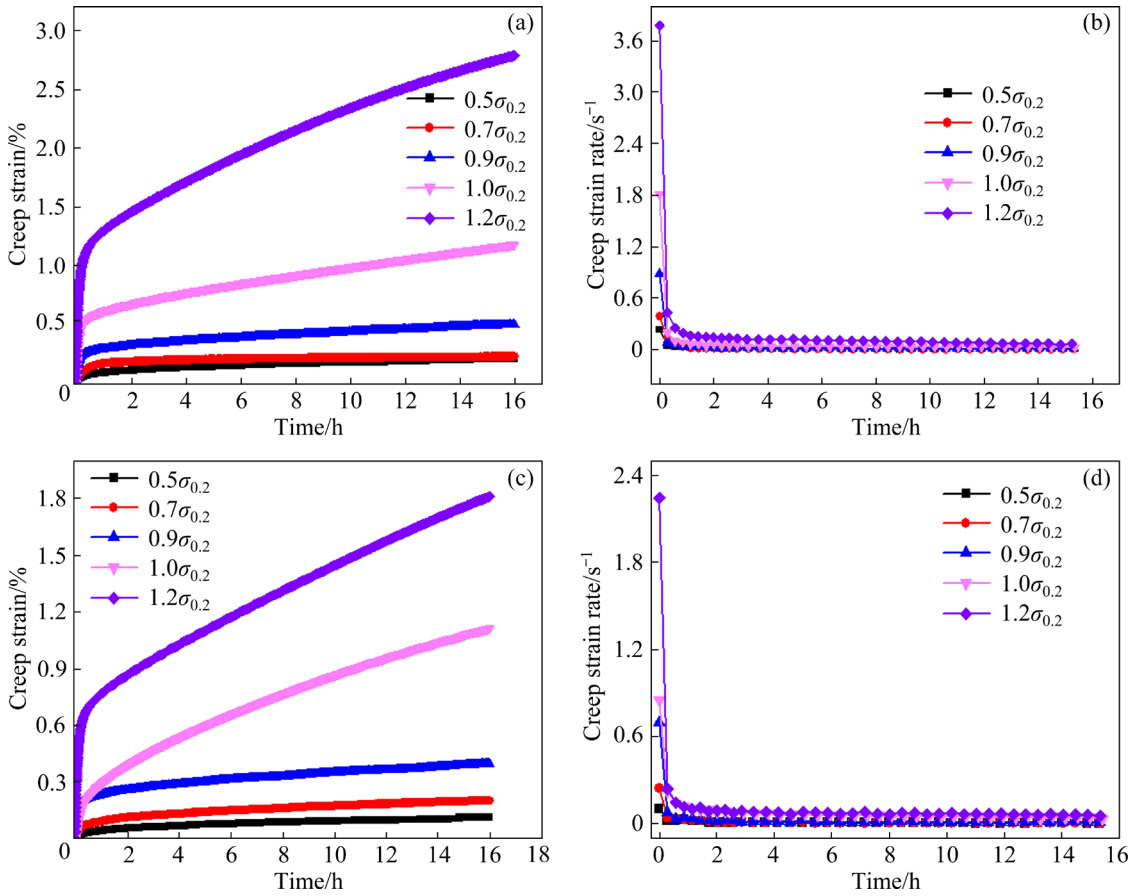

Fig. 6 Creep-aging (a, c) and creep strain rate (b, d) curves of ASR (a, b) and CR (c, d) specimens

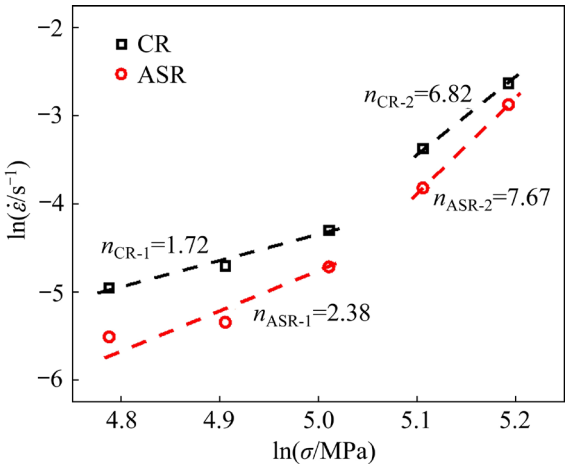

Fig. 7 Steady-strain rate vs stress in natural logarithm with line slope showing stress exponent (n) of creep aging of ASR and CR specimens

the ASR specimens notably increased with the initial creep stress. At a stress level of 0.5$\sigma_{0.2}$, the UTS and YS of the ASR specimens reached 525 and 338 MPa, respectively, whereas those of the CR specimens were 498 and 312 MPa, respectively. Notably, the UTS of the ASR specimens increased by 27 MPa, and the YS increased by 26 MPa compared to those of the CR specimens. Remarkably, the ASR samples exhibited superior overall mechanical properties compared to the CR specimens.

3.4 Microstructure after creep-aging

EBSD analysis provided deeper insights into grain orientation and spatial distribution. Figures 9 and 10 depict the inverse pole figure (IPF) diagram, grain size distribution, and orientation angle distribution of both ASR and CR specimens following creep-aging under various initial creep stresses, respectively. The grain size, the extent of the recrystallization, and the crystal orientation observed in both ASR and CR specimens after creep aging exhibit similarities to those treated with the solution process. In both ASR and CR specimens subjected to various creep stresses, the majority of equiaxed grains were observed, indicating that the degree of recrystallization remained consistent following creep aging. However, the ASR samples demonstrated a more

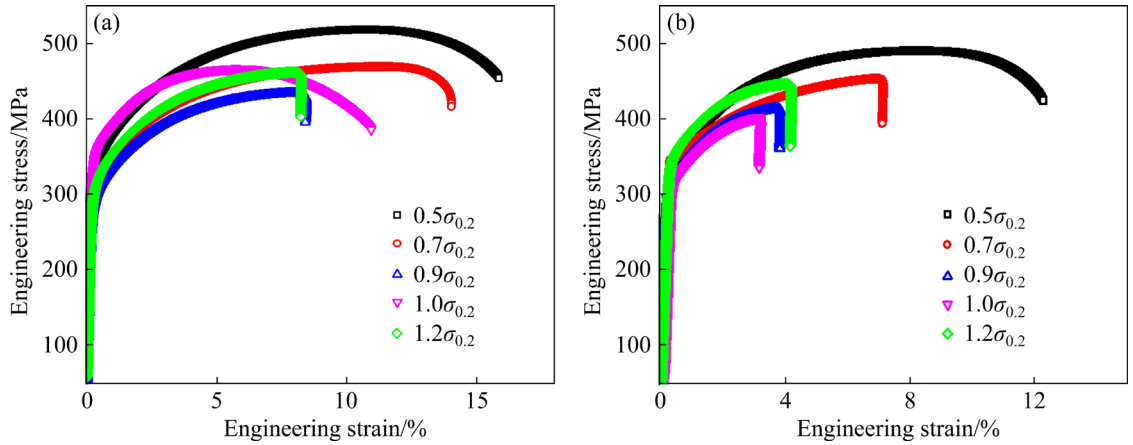

Fig. 8 Mechanical properties of ASR (a) and CR (b) specimens creep-aged at 160 °C and various creep stresses

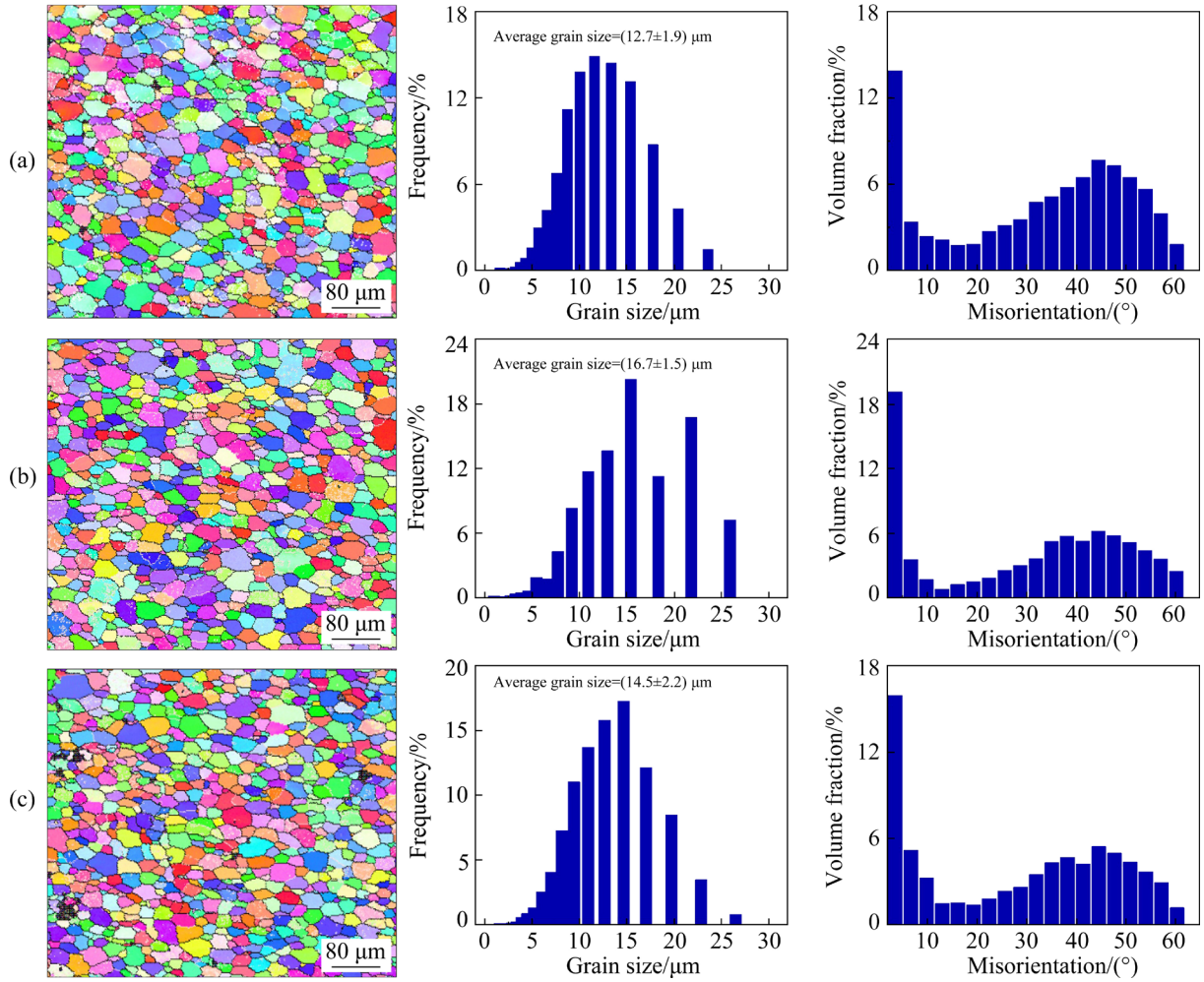

Fig. 9 IPF diagrams, and distributions of grain size and recrystallization degree of ASR-$0.5\sigma_{0.2}$ (a), ASR-$0.7\sigma_{0.2}$ (b), and ASR-$1.2\sigma_{0.2}$ (c) specimens

uniform distribution of grain sizes with finer equiaxed grains. Interestingly, in the ASR samples, smaller grains seemed to be sandwiched between larger ones, indicating a non-uniform distribution of grains. The grain sizes of ASR specimens under creep stresses of $0.5\sigma_{0.2}$, $0.7\sigma_{0.2}$, and $1.2\sigma_{0.2}$ were measured to be 12.7, 16.7, and 14.5 μm, respectively. Similarly, for CR specimens under creep stresses of $0.5\sigma_{0.2}$, $0.7\sigma_{0.2}$, and $1.2\sigma_{0.2}$, the grain sizes were determined as 18.4, 19.6, and 18.5 μm,

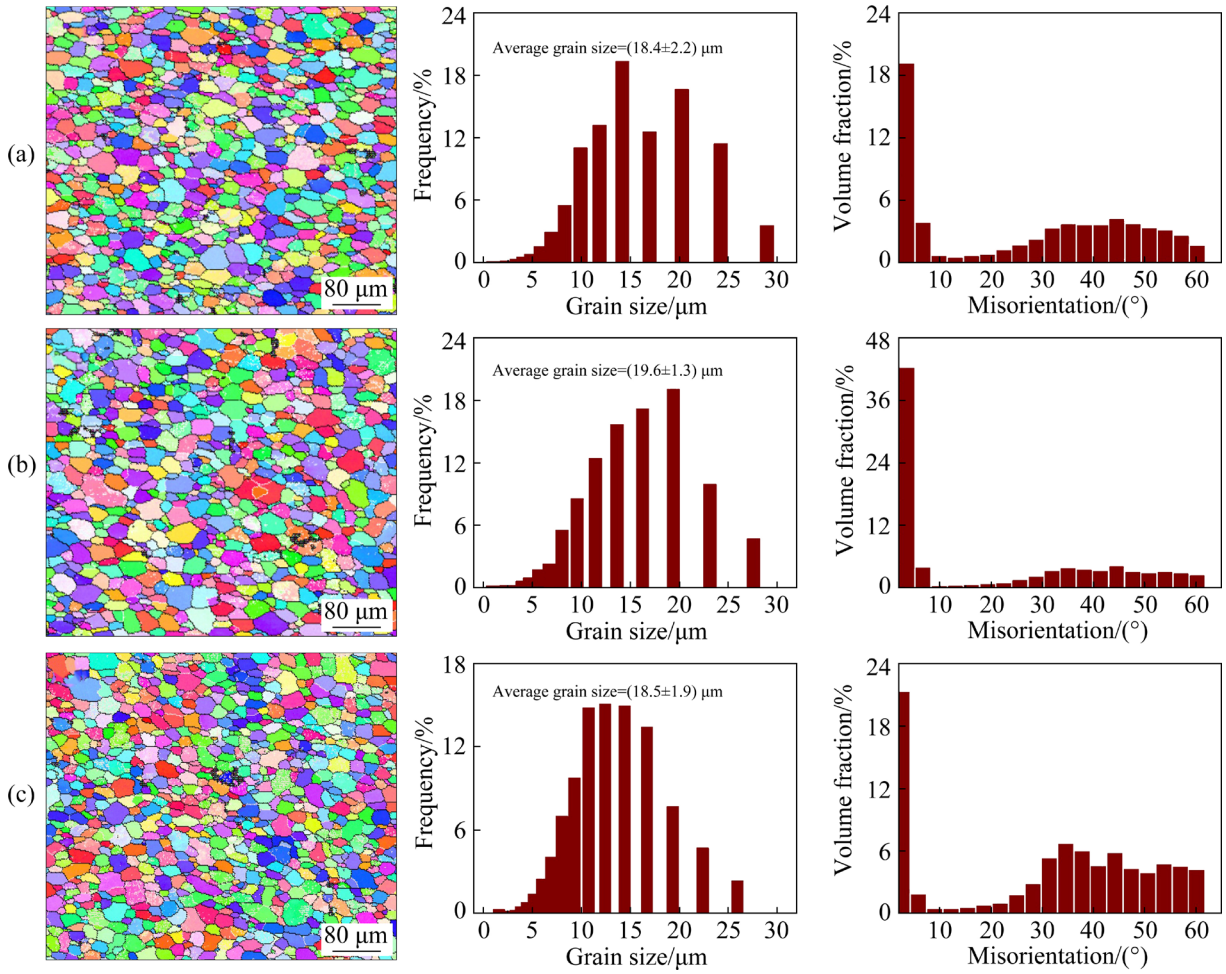

Fig. 10 IPF diagrams, and distributions of grain size and recrystallization degree of CR-0.5$\sigma_{0.2}$ (a), CR-0.7$\sigma_{0.2}$ (b), and CR-1.2$\sigma_{0.2}$ (c) specimens

respectively. Remarkably, the grain sizes of the creep-aged samples remained at similar levels to those of specimens subjected to solid solution treatment. This suggests that the grain sizes of both CR and ASR specimens remained unchanged throughout the creep aging process.

Figures 9 and 10 depict the misorientation distribution of ASR and CR specimens, respectively. The volume fraction of HAGBs in ASR specimens subjected to creep stresses of 0.5$\sigma_{0.2}$, 0.7$\sigma_{0.2}$, and 1.2$\sigma_{0.2}$ was determined to be 76.6%, 74.5%, and 80.5%, respectively. Similarly, the volume fraction of HAGBs in CR specimens under creep stresses of 0.5$\sigma_{0.2}$, 0.7$\sigma_{0.2}$, and 1.2$\sigma_{0.2}$ was determined to be 75.8%, 74.9%, and 74.3%, respectively. Compared with the solid-solution specimens, it is evident that the orientation distribution of the samples after creep aging remains very similar, regardless of the magnitude of the applied creep stress.

Figures 11(a−f) demonstrate low magnification microscopy STEM images taken along the $[110]_{Al}$ zone axis of CR and ASR specimens following 16 h of creep-aging under various initial creep stresses. According to the EDS results of ASR-0.7$\sigma_{0.2}$ specimen in Fig. 11(g), the precipitates primarily consisted of Guinier−Preston (GP) zones, θ'' (Al_3Cu) phases, and θ' (Al_2Cu) phases [31,32]. Due to the semi-coherent nature of these phases with the matrix, dislocations are unable to shear through the θ' and θ'' phases directly. Instead, they typically bypass these obstacles in accordance with the Orowan mechanism [33].

However, dislocations can traverse GP zones and coherent θ'' phase. Consequently, the presence of θ' phase notably enhances the mechanical performance of the Al−Cu alloy during aging by effectively obstructing dislocation motion. The image depicted in Fig. 11 was obtained along the

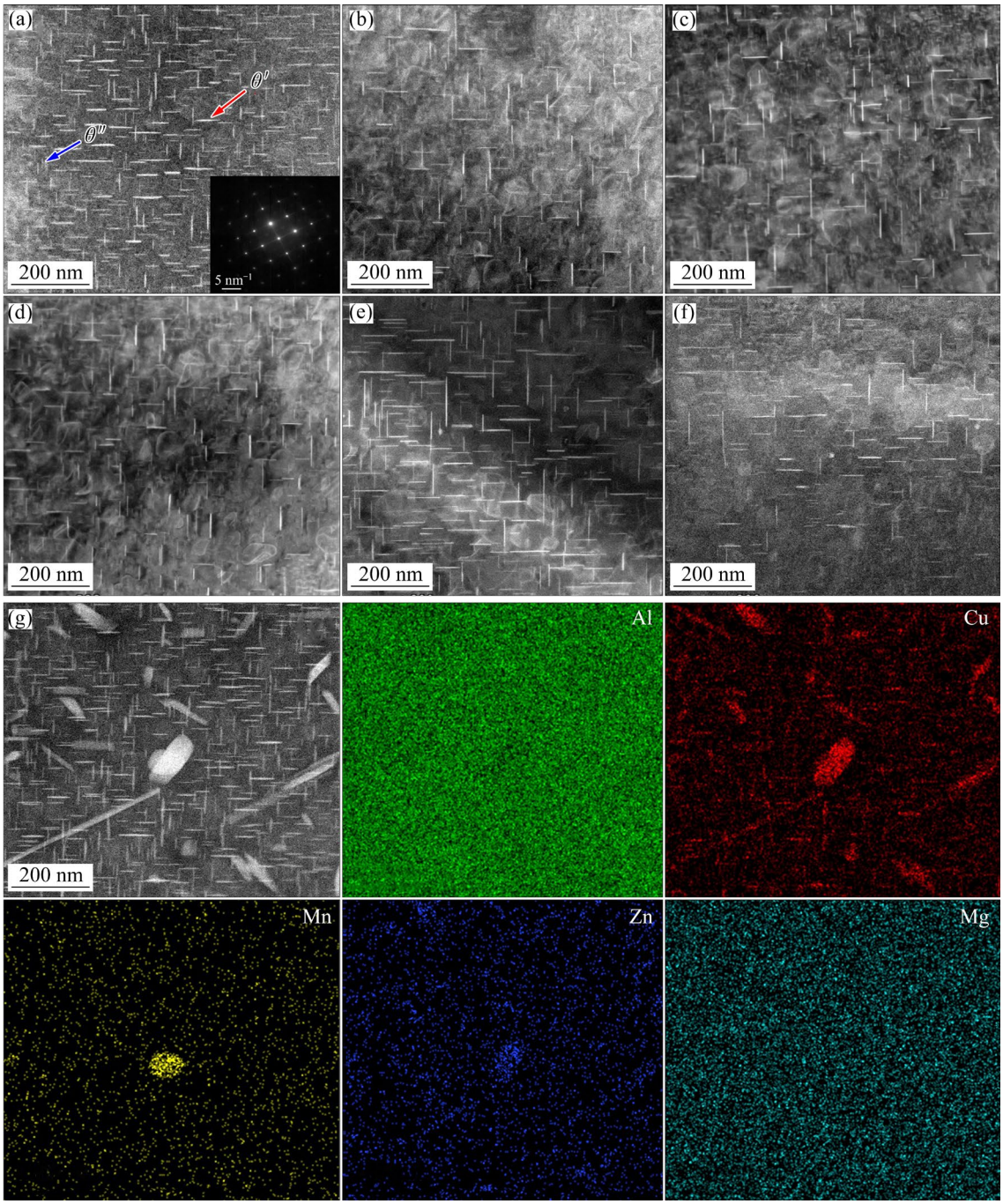

Fig. 11 Low-magnification STEM images of ASR-0.5$\sigma_{0.2}$ (a), ASR-0.7$\sigma_{0.2}$ (b), ASR-1.2$\sigma_{0.2}$ (c), CR-0.5$\sigma_{0.2}$ (d), CR-0.7$\sigma_{0.2}$ (e), and CR-1.2$\sigma_{0.2}$ (f) specimens; (g) EDS results of ASR-0.7$\sigma_{0.2}$ specimen

⟨001⟩ zone axis, allowing for the observation of the θ' phase, as highlighted by the red arrow. Furthermore, the HAADF-STEM image captured the θ'' phase with high density, indicated by the blue arrow, which displayed clear diffraction patterns. To explore the impact of various applied stresses, STEM imaging was conducted on ASR and CR specimens (Fig. 11). It was noted that, following 16 h of creep-aging, two distinct phases emerged: a greater quantity of finely dispersed θ'' phase and larger-sized θ' phase.

Additionally, we analyzed the sizes of the θ' phases to evaluate how different applied stresses affect the distribution of precipitates formed during the creep-aging. STEM images were obtained to evaluate the average diameter distribution of θ' precipitates in specimens subjected to aging of ASR and CR at room temperature, as illustrated in Fig. 12. To ensure the accuracy of quantitative analysis, we utilized at least five images to manually

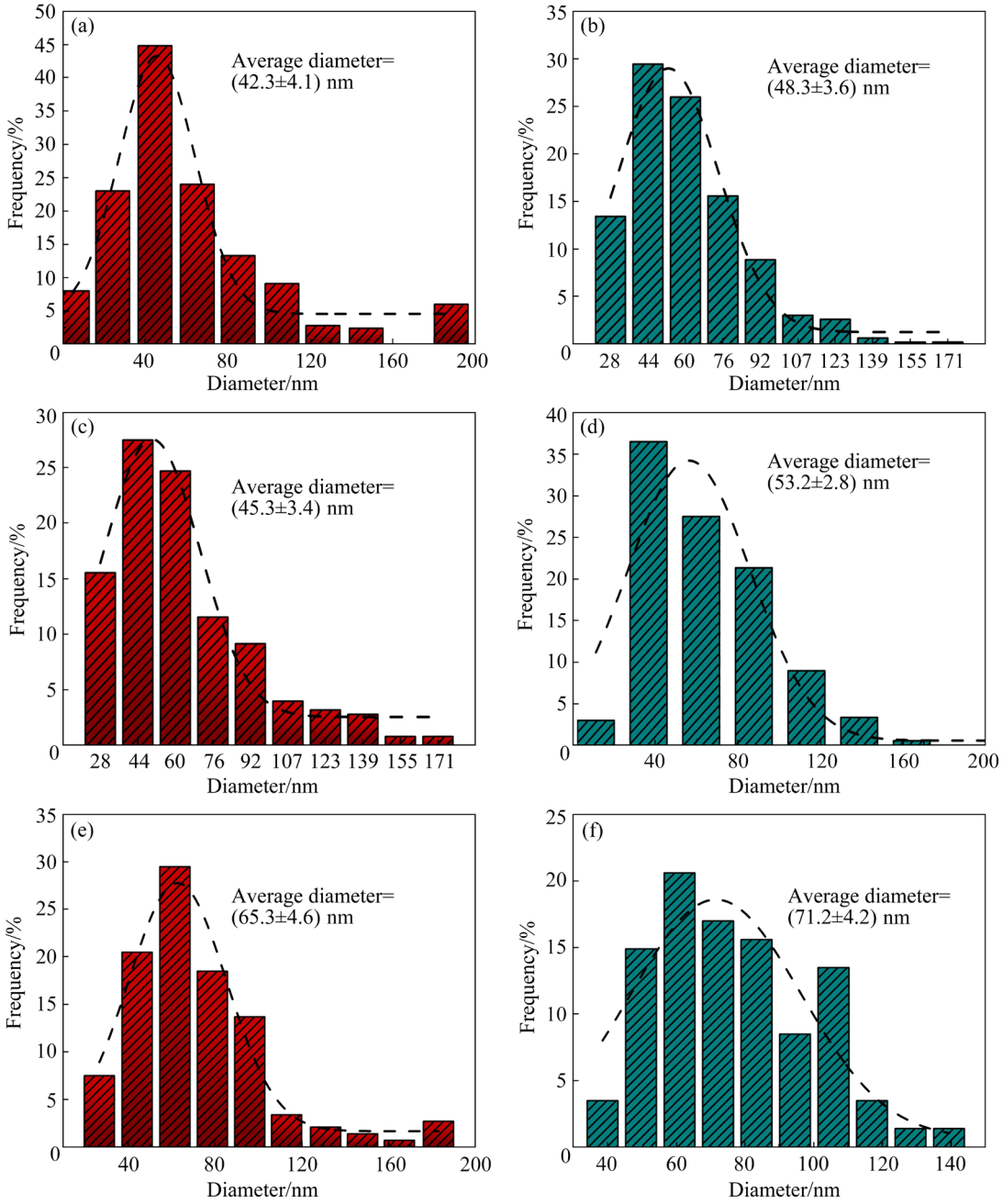

Fig. 12 θ' phase diameter distributions of ASR and CR specimens after creep-aging: (a) ASR-0.5$\sigma_{0.2}$; (b) CR-0.5$\sigma_{0.2}$; (c) ASR-0.7$\sigma_{0.2}$; (d) CR-0.7$\sigma_{0.2}$; (e) ASR-1.2$\sigma_{0.2}$; (f) CR-1.2$\sigma_{0.2}$

ascertain the size and distribution of θ' precipitates under various experimental conditions. To reduce statistical discrepancies, the average diameter of θ' precipitates was determined based on three sets of statistical data obtained for each image. As depicted in Fig. 12, the average diameter of θ' phases in ASR specimens under the creep stresses of 0.5$\sigma_{0.2}$, 0.7$\sigma_{0.2}$, and 1.2$\sigma_{0.2}$ was 42.3, 45.3, and 65.3 nm, respectively. In contrast, the average diameter of θ' phases in CR specimens under the same creep stresses of 0.5$\sigma_{0.2}$, 0.7$\sigma_{0.2}$, and 1.2$\sigma_{0.2}$ was 48.3, 53.2 and 71.2 nm, respectively. Notably, the average diameter of θ' phases in ASR specimens decreased significantly by 6.0, 7.9, and 5.9 nm compared to that of CR specimens under creep stresses of 0.5$\sigma_{0.2}$, 0.7$\sigma_{0.2}$, and 1.2$\sigma_{0.2}$, respectively.

For a more precise determination of the thickness of θ' phases, we conducted calculations using higher magnification images of the three samples. Figure 13 presents the HRTEM images of θ' phases in the three specimens, where the thickness of θ' phases was measured using Image J

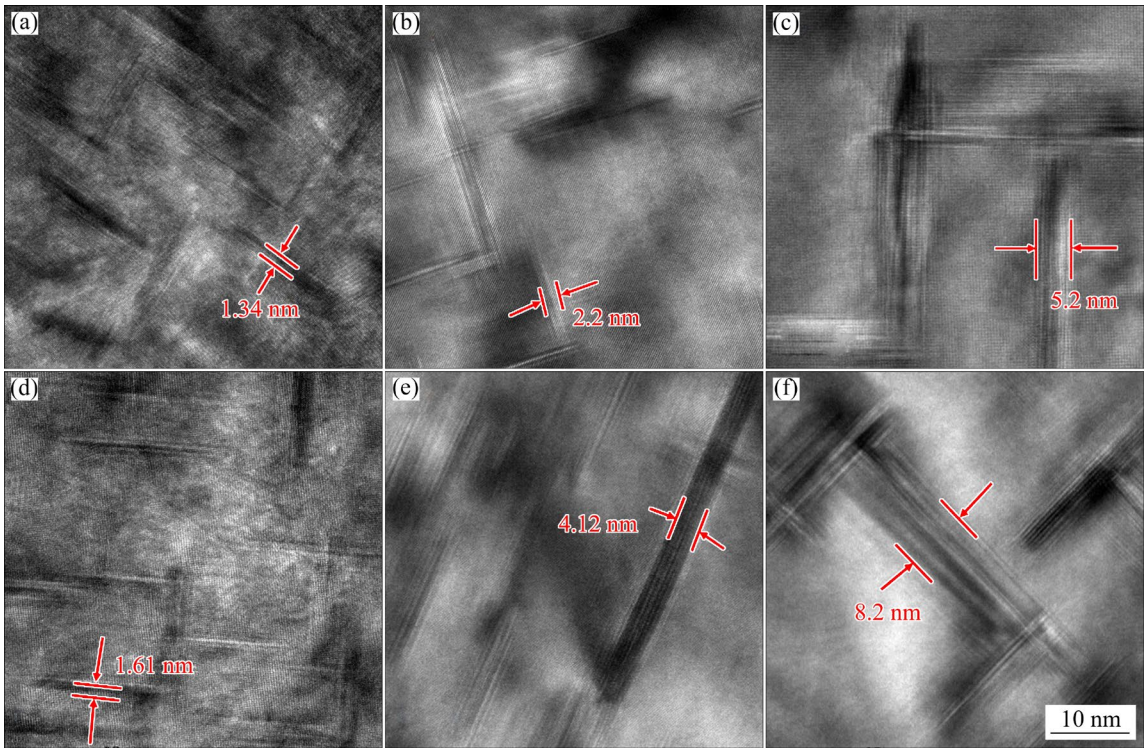

Fig. 13 HRTEM images of ASR and CR specimens after creep-aging: (a) ASR-0.5$\sigma_{0.2}$; (b) ASR-0.7$\sigma_{0.2}$; (c) ASR-1.2$\sigma_{0.2}$; (d) CR-0.5$\sigma_{0.2}$; (e) CR-0.7$\sigma_{0.2}$; (f) CR-1.2$\sigma_{0.2}$

software. Based on the statistical analysis, the thickness of θ' phases in the ASR sample was found to be narrower compared to that of the CR samples. After accounting for potential testing errors, the thickness of θ' phases in the ASR sample was determined to be 1.34 nm under an applied stress of 0.5$\sigma_{0.2}$. In comparison, the θ' phases in the CR sample showed a thickness of 1.61 nm under the same applied stress condition. It is worth noting that the thickness of θ' phases is affected by the applied stress, with an increase in applied stress, resulting in a corresponding increase in the thickness of θ' phases.

4 Discussion

4.1 Creep deformation of ASR and CR specimens

The primary factors influencing dislocation density are the mechanisms of dislocation multiplication and annihilation. Currently, the evaluation of dislocation density through EBSD involves categorizing dislocations into two groups: statistically stored dislocations (SSDs) and geometrically necessary dislocations (GNDs). When assessing dislocation density, GNDs hold particular significance for aluminum alloys due to their increased dislocation energy. The determination of GNDs at each measurement point involves averaging the local disorientation (θ_{ij}) over neighboring pixels j, situated at a fixed distance from the pixel i being considered. The calculation of dislocation density, denoted as ρ_{GND}, is calculated by [25]

$$\rho_{GND}=\frac{\alpha\langle\theta_{ij}\rangle}{bx} \tag{3}$$

In this equation, α represents a constant dependent on the type of dislocations (whether they are edge or screw dislocations). For this study, a value of α=3 was suggested [26]. The term $\langle\theta_{ij}\rangle$ signifies the average value of θ_{ij}, corresponding to the kernel average misorientation angle (KAM) when considering the peripheral pixels of the kernel. The magnitude of the Burgers vector of dislocations is denoted by b, and x denotes the distance over which $\langle\theta_{ij}\rangle$ is calculated. In the EBSD data processing software packages, the KAM is commonly utilized as a surrogate for the following equation [27]:

$$\rho=\alpha\frac{\mathrm{KAM}}{bR} \tag{4}$$

The KAM values, which provide information about the average misorientation angle, are obtained through the EBSD software. When generating KAM maps, the kernel size (R) is considered to encompass neighboring orders.

Table 3 displays the KAM values, which can be utilized to evaluate the energy storage within the deformed microstructure. The strain energy stored per unit volume (E) can be calculated by [28]

$$E=\frac{1}{2}G\rho b^2 \tag{5}$$

The geometrically necessary dislocation density ρ_{GND} and strain energy stored per unit volume E of the CR and ASR specimens were calculated using the previous equation, considering the shear modulus (G) of aluminum, which is 26.1 GPa [29].

Table 3 Forest dislocation density and strain energy in ASR and CR specimens after solution treatment

Aging condition	Dislocation density/10^{14} m^{-2}				
	CR-top	CR-mid	ASR-top	ASR-mid	ASR-bot
T4	1.24	1.19	1.44	1.28	1.25
$0.5\sigma_{0.2}$	0.31	0.31	0.43	0.43	0.43
$0.7\sigma_{0.2}$	0.35	0.35	0.49	0.49	0.49
$1.2\sigma_{0.2}$	0.38	0.38	0.54	0.54	0.54
Aging condition	Strain energy/(J·m^{-3})				
	CR-top	CR-mid	ASR-top	ASR-mid	ASR-bot
T4	1.45	1.39	1.69	1.51	1.47
$0.5\sigma_{0.2}$	0.37	0.37	0.51	0.51	0.51
$0.7\sigma_{0.2}$	0.41	0.41	0.58	0.58	0.58
$1.2\sigma_{0.2}$	0.45	0.45	0.63	0.63	0.63

Based on the results presented in Section 3.2, the creep strain of both the CR and ASR specimens was assessed under various applied stresses. The results indicate that the total creep strain of the ASR specimens exceeds that of the CR specimens under different stress conditions. This discrepancy can be attributed to various factors, including dislocation density, precipitate formation, and texture orientation, all of which collectively contribute to the increased creep rate observed in the ASR specimens during the initial stage of creep strain.

Previous studies [8] have indicated that the accumulation of dislocation motion plays a crucial role in creep strain. In aluminum matrices characterized by a high density of dislocations, dislocations are more prone to slip and climb readily, thereby facilitating the movement associated with creep strain [34]. As shown in Table 3, the ASR specimens exhibited a higher initial dislocation density compared to the CR specimens. Consequently, the ASR specimens displayed a significantly higher initial creep strain rate than the CR specimens, resulting in an elevated creep strain magnitude in the ASR specimens relative to the CR specimens.

The alignment of the Al matrix texture plays a vital role in shaping its deformation characteristics [35]. Recrystallized texture is mainly composed of Cube textures [36]. In both ASR and CR samples, Goss textures were observed as the main recrystallized textures. Illustrated in Fig. 5, the CR samples primarily exhibited Goss and Copper textures, although with a small amount of Cube textures compared to the ASR samples. The findings distinctly show a greater occurrence of recrystallized textures in the ASR specimens than in the CR samples. Typically, a high occurrence of recrystallized textures is advantageous for the creep aging strain properties of the alloy [22]. Based on these results, it can be deduced that the ASR sample exhibited a significantly higher prevalence of recrystallized textures compared to the CR sample, indicating superior creep strain characteristics of the ASR sample.

Creap strain in aluminum alloy sheets can be affected by several factors, such as grain size, dislocation density, crystal orientation, and grain boundaries. Among these, crystal orientation plays a vital role in shaping formability [37]. Therefore, ASR results in grain refinement and promotes recrystallization. These results demonstrate that the deformation mode and subsequent recrystallization process of ASR affect the texture arrangement of the alloy, especially the distribution of Cube textures. This fine-tuning of the texture arrangement helps improve the creep strain of 2219 aluminum alloy sheets to some extent.

4.2 Mechanical properties of ASR and CR specimens

The yield strength of materials can be determined by thoroughly analyzing microstructural features, including textures, forest dislocation

density, and precipitates [38]. These factors also have a considerable impact on the mechanical properties of materials [39]. Expanding on previous research, the yield strength of 2219 aluminum alloy can be ascribed to the collective influences of solid solution strengthening, precipitation hardening, and dislocation mechanisms. It can be calculated as follows [40]:

$$\Delta\sigma=\sigma_0+\sigma_{ss}+\sqrt{\sigma_\rho^2+\sigma_{ppt}^2} \tag{6}$$

In Eq. (6), the yield strength of pure aluminum (σ_0=35 MPa) was taken into account. Here, σ_{ss} represents the strength attributed to the solid solution strengthening, and σ_{ppt} signifies the strength factor related to the precipitation hardening. Earlier investigation [29] has suggested that σ_{ss} can be approximated as 27 MPa. Furthermore, the strengthening arising from the dislocation density, represented as σ_ρ, can be calculated as follows [41]:

$$\sigma_\rho=M\alpha Gb\rho^{1/2} \tag{7}$$

The dislocation density contribution σ_ρ in Eq. (7) depends on several factors, including the Taylor factor (M), shear modulus G, magnitude of Burgers vector b, and dislocation density ρ, with a constant α typically around 0.3. Table 3 presents the dislocation densities for both ASR and CR specimens in the creep-aging state. In this study, both ASR and CR specimens underwent solution treatment without pre-deformation, followed by creep aging, resulting in a lower dislocation density compared to pre-deformed samples. Hence, it can be deduced that the contribution of dislocations is similar for both ASR and CR samples. Using Eq. (7), the dislocation hardening can be calculated by considering the elevated dislocation density and the corresponding changes in the M values. The M values can be determined using various models, such as the Sachs model, Taylor model, and Hutchinson's self-consistent model, depending on the number of slip systems [42]. Table 4 displays the calculated M values for ASR and CR specimens using three distinct models. It was noted that the M values for ASR specimens surpassed those for CR specimens. This indicates a notable influence of recrystallization textures on the M values in ASR specimens. Additionally, the dislocation hardening values for ASR and CR specimens can be determined using Eq. (7), as illustrated in Table 3. It is important to highlight that the calculated dislocation hardening value is higher in ASR specimens compared to that in CR specimens. This difference could be attributed to variations in the M value and dislocation density between ASR and CR samples. The increased contribution of dislocations to the overall strength is influenced by the M value (Table 4) and the intensity of dislocation. Furthermore, Table 3 also presents the outcomes of dislocation density calculations for CR and ASR specimens under different aging conditions.

Table 4 Average M values of ASR and CR specimens after solution treatment

Specimen	Taylor model (5 systems)	Sach model (1 system)	Hutchinson's self-consistent model (3.5 systems)
ASR	3.09	2.45	2.81
CR	3.07	2.36	2.75

It is indicated that the interaction between the precipitates (θ' and θ'' phases) and dislocations directly affects the precipitation hardening (σ_{ppt}) of the 2219 aluminum alloy. This interaction can be quantitatively described by [43]

$$\sigma_{ppt}^{1.4}=\sigma_{shearable}^{1.4}+\sigma_{shear\text{-}resistant}^{1.4} \tag{8}$$

where $\sigma_{shearable}$ denotes the shear precipitate hardening induced by dislocations cutting through the θ'' phase during deformation. The expression for this strengthening component can be expressed as follows [29]:

$$\sigma_{shearable}=M\beta\frac{0.928D_{\theta''}}{T_{\theta''}}\left(\frac{bf_{\theta''}f_{ma}}{\Gamma}\right)^{1/2}\gamma_i^{3/2} \tag{9}$$

where β signifies the stress orientation factor, $D_{\theta''}$ stands for the average diameter of θ'' precipitates, $T_{\theta''}$ denotes the thickness of θ'' phases, f_{ma} represents the maximum absolute volume fraction of θ'' phases, $f_{\theta''}$ represents the volume fraction of θ'' phases, γ_i represents the interfacial energy between θ'' phases and the Al matrix, and Γ corresponds to the dislocation line tension [29].

$$\Gamma=Gb^2/(2\pi)\cdot\ln(r_0/r_i) \tag{10}$$

$$r_0=D_{\theta''}/\sqrt{2f_{\theta''}\cdot f_{ma}} \tag{11}$$

The inner and outer cut-off distances are represented by r_i and r_0, respectively. Both the diameter and number density of θ'' phases have a

positive impact on the mechanical properties. Additionally, the thickness of θ'' phases in the aluminum alloy is correlated with its mechanical properties; a greater thickness results in better mechanical properties. During the deformation, dislocations tend to bypass θ' phases, whereas θ' phases are evenly distributed across the three equivalent $\{001\}_{Al}$ planes in the case of 2219 aluminum alloy. The contribution to strengthening can be calculated as follows [44]:

$$\sigma_{\text{shear-resistant}} = M\frac{Gb}{2\pi\sqrt{1-\nu}}\cdot 1/[0.931\sqrt{(0.306\pi D_{\theta'}T_{\theta'})/(f_{\theta'}\cdot f_{\text{ma}})} - (\pi D_{\theta'})/8 - 1.061T_{\theta'}]\cdot\ln\left(\frac{1.225T_{\theta'}}{r_{\text{i}}}\right) \quad (12)$$

The parameters in Eq. (12) comprise ν (Poisson's ratio), $D_{\theta'}$ (average precipitate diameter of θ' phase), $T_{\theta'}$ (thickness of θ' phase), and $f_{\theta'}$ (relative volume fraction of θ' phase). In Al−Cu alloys, the precipitation sequence typically involves the appearance of GP zones followed by the formation of θ'', θ', and θ phases [45]. Earlier studies [46] have thoroughly explored precipitation strengthening mechanisms in Al−Cu alloys, focusing on understanding the interaction between precipitates and dislocations during the deformation process of creep ageing. There is general agreement on the vulnerability of GP zones to shearing by dislocations when situated close to or at the yield strength of the alloy [47].

On the other side, dislocations using Orowan looping mechanisms overcome larger θ'' phases [48]. In certain conditions, when θ' phases are thin (<5 nm) or under high stress (>1 GPa critical resolved shear stress), they can be sheared by dislocations [48,49]. The interaction between precipitates and dislocations in Al−Cu alloys shifts from being primarily controlled by shear to being primarily influenced by bypass mechanisms as the size of the precipitates grows and their coherency reduces [50]. Figures 14(a) and (b) illustrate the schematic progression of the microstructure of the ASR and CR samples during the creep aging. Throughout the process of creep-aged deformation, there is a shift in the behavior of precipitates, transitioning from a shearing mechanism (with θ'' phases) to an Orowan looping mechanism (involving θ' and θ phases) [51]. The ASR samples demonstrate a significantly higher dislocation density compared to the CR samples, thus aiding in the conversion of θ'' phase to θ' phase. As a result, the size of θ' phase in the ASR sample is larger compared to that of the CR sample. In Al−Cu alloys containing a high density of θ' and θ phases, Orowan looping becomes a prominent dislocation bypass mechanism, thus affecting the strain hardening behavior [52]. These alterations in the interactions between precipitates and dislocations have a substantial effect on strain hardening behavior, with Orowan looping emerging as an additional mechanism alongside dislocation tangling, multiplication, and cell formation [53]. Unlike GP zones and θ'' phases, θ' phases are not anticipated to undergo shearing or fracturing. However, they still undergo a certain degree of strain accommodation [54]. Studies conducted by HOSFORD and ZEISLOFT [55] and MISHRA et al [56] have revealed that plate-shaped θ' phases aid shear strain accommodation through rotation due to their high strength and alignment relationship with the matrix. These equations directly clarify the strengthening effects arising from the interaction between dislocation and precipitates. To offer a qualitative description of this influence, Eqs. (9) and (12) are utilized, as depicted in Fig. 14(c). The analysis data are presented in Table 5, which demonstrates the influence of θ' and θ'' phases on the strength enhancement.

In summary, it can be concluded that the mechanical properties of ASR and CR samples were primarily affected by three factors: the type and morphology of the precipitates, the dislocation density, and the crystallographic texture. ASR specimens exhibited smaller precipitate diameters and higher precipitate density than CR specimens. However, there is no significant difference in precipitate thickness between ASR and CR specimens. Precipitates have exhibited stronger strengthening effects in ASR specimens than in CR specimens. The forest dislocation density in ASR specimens was notably higher than that observed in CR specimens. Previous studies have investigated the impact of different texture types on the strength of Al−Cu alloy specimens, identifying Goss and Cube textures as prominent recrystallized textures in both types of specimens. The M value of ASR specimens is lower than that of CR specimens.

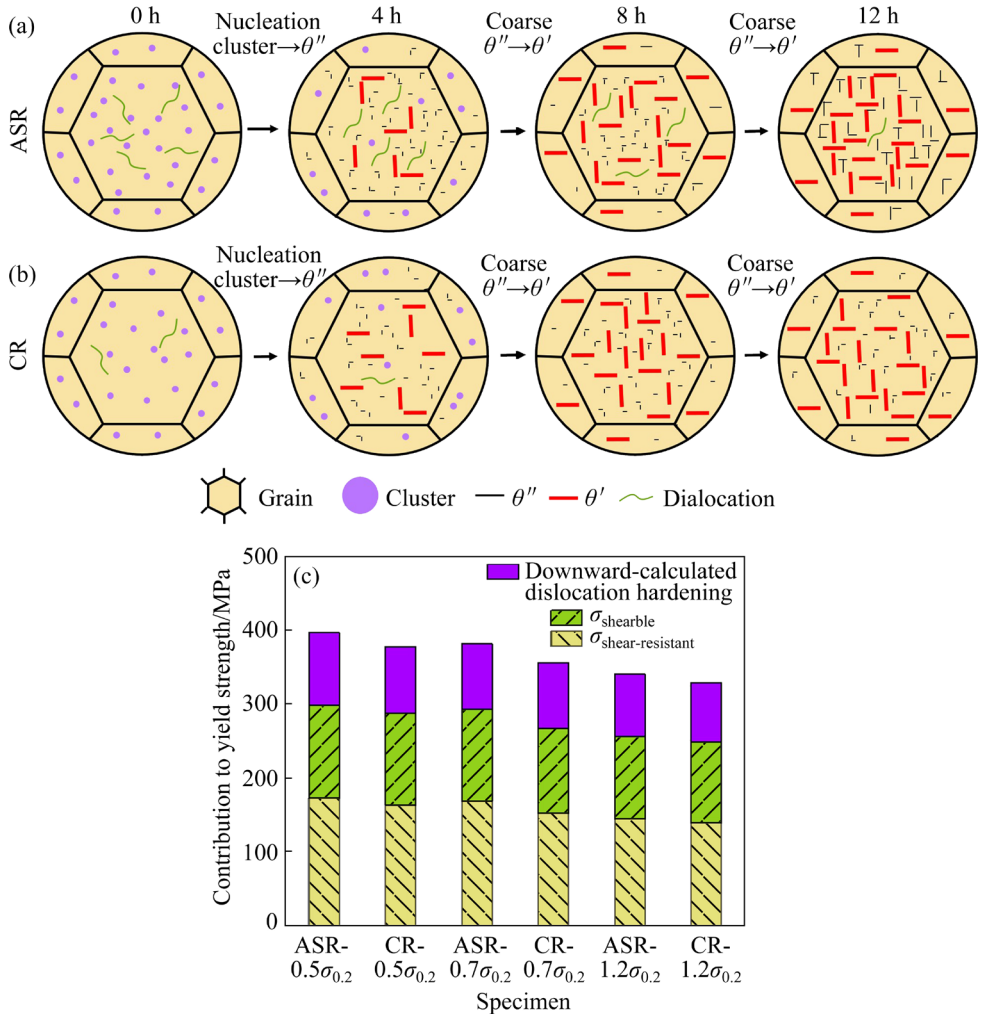

Fig. 14 Schematic progression of microstructure of ASR and CR samples during creep aging (a, b), and contribution to yield strength from precipitation and dislocation hardening (c)

Table 5 Number density and size of θ' and θ'' phases from STEM images in ASR and CR specimens

Specimen	θ' phase			θ'' phase		
	Average thickness/nm	Number density/μm^2	Average diameter/nm	Average thickness/nm	Number density/μm^2	Average diameter/nm
ASR-0.5$\sigma_{0.2}$	1.31	59	43	1.12	51	38
ASR-0.7$\sigma_{0.2}$	4.92	51	56	2.45	46	51
ASR-1.2$\sigma_{0.2}$	6.40	49	83	5.32	36	61
CR-0.5$\sigma_{0.2}$	1.61	52	53	1.36	51	49
CR-0.7$\sigma_{0.2}$	5.20	41	71	3.67	39	58
CR-1.2$\sigma_{0.2}$	8.20	34	107	6.78	30	76

By combining Eqs. (6)−(12) with different strengthening effects, it can be inferred that both precipitates and textures primarily contributed to the strength. Despite the stronger precipitation strengthening in ASR specimens, the difference in yield strength between the two specimens is significant. The strengthening effects from texture in CR specimens were relatively low compared to those of ASR specimens. Additionally, it was noted that the mechanical properties of both ASR and CR specimens declined with increasing creep stress. This can be attributed to the stress orientation effect

of precipitates, which negatively affects aging hardening, as depicted in Fig. 11. The STEM images (Fig. 11) revealed the presence of distinct θ' and θ'' phases on both ASR and CR specimens. The stress orientation effect occurs when the stress field surrounding the dislocation surpasses the externally applied stress by a considerable margin. This results in an adverse stress effect and the enlargement of the precipitated phase within the specimens.

5 Conclusions

(1) At a stress level of $1.2\sigma_{0.2}$, ASR samples exhibit 50% higher creep strain than CR specimens, leading to increased strength but reduced plasticity. At a stress level of $0.5\sigma_{0.2}$, ASR specimens show slight advantages in both strength and plasticity over CR specimens.

(2) At a stress level of $0.5\sigma_{0.2}$, ASR specimens exhibit a UTS that is 27 MPa greater and a YS that is 26 MPa greater than those of CR specimens. The elongation for ASR and CR is 12.1% and 7.2%, respectively. Following 16 h of creep aging at $1.2\sigma_{0.2}$, ASR demonstrates a creep strain of 2.86% compared to 1.91% for CR, highlighting the superior mechanical properties and creep aging performance of ASR specimens.

(3) ASR specimens resulted in finer precipitates and more recrystallized grains than CR specimens, beneficial to creep deformation. The average diameters of θ' phases in ASR specimens under stresses of $0.5\sigma_{0.2}$, $0.7\sigma_{0.2}$, and $1.2\sigma_{0.2}$ are increased by 6.0, 7.9, and 5.9 nm, respectively, compared to CR specimens. ASR specimens have smaller average diameters of θ' and θ'' phases and smaller grain sizes (13.5 μm) than CR specimens (18.9 μm). ASR also shows higher M values. Differences in creep aging behavior between ASR and CR are due to texture and forest dislocation density. ASR specimens show more cube textures and higher recrystallization, leading to increased creep strain. Forest dislocation density is higher in ASR ($1.32\times10^{14}\,m^{-2}$) than in CR ($1.21\times10^{14}\,m^{-2}$), contributing to elevated creep strain. Texture, forest dislocation density, and precipitation characteristics are key factors in strength differences. ASR specimens display higher M values and increased yield strength after creep-ageing due to higher number density and average diameter of θ' and θ'' phases.

CRediT authorship contribution statement

Quan-qing ZENG: Conceptualization, Data curation, Formal analysis, Investigation, Writing – Original draft; **Dong-yao WANG:** Investigation, Validation; **Bo-lin MA:** Investigation, Project administration, Supervision, Experimental equipment; **Yong-qian XU:** Investigation, Methodology; **Ming-hui HUANG, Lei TANG, Chang-zhi LIU,** and **Dong-yang YAN:** Investigation, Experimental equipment; **Li-hua ZHAN** and **You-liang YANG:** Conceptualization, Funding acquisition, Supervision, Writing – Review & editing.

Declaration of competing interest

The authors declare that they have no known competing financial interests or personal relationships that could have appeared to influence the work reported in this paper.

Acknowledgments

The authors would like to thank for the financial supports from the National Key Research and Development Program of China (No. 2021YFB3400900), the National Natural Science Foundation of China (Nos. U22A20190, U2341273, 52205435), the Natural Science Foundation of Hunan Province, China (No. 2022JJ40621), the Science and Technology Innovation Program of Hunan Province, China (No. 2020RC4001), and the Project of State Key Laboratory of Precision Manufacturing for Extreme Service Performance, Central South University, China (No. ZZYJKT2022-07). The authors would like to express their gratitude to EditSprings (https://www.editsprings.cn) for the expert linguistic services provided.

References

[1] ZHANG Jin, DENG Yun-lai, LI Si-yu, CHEN Ze-yu, ZHANG Xin-ming. Creep age forming of 2124 aluminum alloy with single/double curvature [J]. Transactions of Nonferrous Metals Society of China, 2013, 23(7): 1922−1929.

[2] KHANI M S, KAZEMINEZHAD M. Effects of non-isothermal annealing on microstructure and mechanical properties of severely deformed 2024 aluminum alloy [J]. Transactions of Nonferrous Metals Society of China, 2017, 27(1): 1−9.

[3] RANA A S, JOSHI A, CHAMOLI S, KANAWAT C S, PANT P K. Optimization of WEDM process parameters for machining Al 2219 alloy [J]. Materials Today: Proceedings, 2020, 26: 2541−2545.

[4] MILLIGAN B K, ROY S, HAWKINS C S, ALLARD L F, SHYAM A. Impact of microstructural stability on the creep behavior of cast Al−Cu alloys [J]. Materials Science and Engineering: A, 2020, 772: 138697.

[5] LUMLEY R N, MORTON A J, POLMEAR I J. Enhanced creep performance in an Al−Cu−Mg−Ag alloy through underageing [J]. Acta Materialia, 2002, 50(14): 3597−3608.

[6] ARABI J R, EMAMI M, SHAHVERDI H R, HADAVI S M M. Effects of time and temperature on the creep forming of 7075 aluminum alloy: Springback and mechanical properties [J]. Materials Science and Engineering: A, 2011, 528(29/30): 8795−8799.

[7] LI Mao-hua, YANG Yan-qing, FENG Zong-qiang, HUANG Bin, LUO Xian, LOU Ju-hong, RU Ji-gang. Precipitation sequence of η phase along low-angle grain boundaries in Al−Zn−Mg−Cu alloy during artificial aging [J]. Transactions of Nonferrous Metals Society of China, 2014, 24(7): 2061−2066.

[8] LAM A C, SHI Zhu-sheng, YANG Hao-liang, WAN Li, DAVIES C M, LIN Jian-guo, ZHOU Shi-jie. Creep-age forming AA2219 plates with different stiffener designs and pre-form age conditions: Experimental and finite element studies [J]. Journal of Materials Processing Technology, 2015, 219: 155−163.

[9] ARABI J R, ZOHDI H, SHAHVERDI H R, BOZORG M, HADAVI S M M. Influence of multi-step heat treatments in creep age forming of 7075 aluminum alloy: Optimization for springback, strength and exfoliation corrosion [J]. Materials Characterization, 2012, 73: 8−15.

[10] WANG Qing, ZHAN Li-hua, XU Yong-qian, LIU Chun-hui, ZHAO Xing, XU Ling-zhi, YANG You-liang, CAI Yi-xian. Creep aging behavior of retrogression and re-aged 7150 aluminum alloy [J]. Transactions of Nonferrous Metals Society of China, 2020, 30(10): 2599−2612.

[11] XU Yong-qian, ZHAN Li-hua, XU Ling-zhi, HUANG Ming-hui. Experimental research on creep aging behavior of Al−Cu−Mg alloy with tensile and compressive stresses [J]. Materials Science and Engineering: A, 2017, 682: 54−62.

[12] SANTECCHIA E, CABIBBO M, GHAT M, REGEV M, SPIGARELLI S. Physical modeling of the creep response of an Al−Cu−Mg alloy with a fine microstructure transformed by friction stir processing [J]. Materials Science and Engineering: A, 2020, 769: 138521.

[13] XU Yong-qian, ZHAN Li-hua, MA Zi-yao, HUANG Ming-hui, WANG Kai, SUN Zhao. Effect of heating rate on creep aging behavior of Al−Cu−Mg alloy [J]. Materials Science and Engineering: A, 2017, 688: 488−497.

[14] CHEN Xue-ying, ZHAN Li-hua, MA Zi-yao, XU Yong-qian, ZHENG Qiang, CAI Yi-xian. Study on tensile/compressive asymmetry in creep ageing behavior of Al−Cu alloy under different stress levels [J]. Journal of Alloys and Compounds, 2020, 843: 156157.

[15] LIU Chun-hui, YANG Jian-shi, MA Pei-pei, MA Zi-yao, ZHAN Li-hua, CHEN Kai-liang, HUANG Ming-hui, LI Jian-jun, LI Zhi-ming. Large creep formability and strength–ductility synergy enabled by engineering dislocations in aluminum alloys [J]. International Journal of Plasticity, 2020, 134: 102774.

[16] BINTU A, VINCZE G, PICU R C, LOPES A B. Effect of symmetric and asymmetric rolling on the mechanical properties of AA5182 [J]. Materials & Design, 2016, 100: 151−156.

[17] SIDOR J, MIROUX A, PETROV R, KESTENS L. Controlling the plastic anisotropy in asymmetrically rolled aluminium sheets [J]. Philosophical Magazine, 2008, 88(30/31/32): 3779−3792.

[18] JI Y H, PARK J J. Development of severe plastic deformation by various asymmetric rolling processes [J]. Materials Science and Engineering: A, 2009, 499(1/2): 14−17.

[19] AMEGADZIE M Y, BISHOP D P. Effect of asymmetric rolling on the microstructure and mechanical properties of wrought 6061 aluminum [J]. Materials Today Communications, 2020, 25: 101283.

[20] MAGALHÃES D C C, KLIAUGA A M, FERRANTE M, SORDI V L. Asymmetric cryorolling of AA6061 Al alloy: Strain distribution, texture and age hardening behavior [J]. Materials Science and Engineering: A, 2018, 736: 53−60.

[21] SHI Chen, MAO Da-heng, FU Zong-li. Asymmetric cast-rolling of 1050 aluminum alloy strip under multi-energy field [J]. Transactions of Nonferrous Metals Society of China, 2014, 24(9): 2815−2823.

[22] SAKAI T, BELYAKOV A, KAIBYSHEV R, MIURA H, JONAS J J. Dynamic and post-dynamic recrystallization under hot, cold and severe plastic deformation conditions [J]. Progress in Materials Science, 2014, 60: 130−207.

[23] ZUO Yu-bo, FU Xing, CUI Jian-zhong, TANG Xiang-yu, MAO Lu, LI Lei, ZHU Qing-feng. Shear deformation and plate shape control of hot-rolled aluminium alloy thick plate prepared by asymmetric rolling process [J]. Transactions of Nonferrous Metals Society of China, 2014, 24(7): 2220−2225.

[24] LEE J H, KIM G H, NAM S K, KIM I, LEE D N. Calculation of plastic strain ratio of AA1050 Al alloy sheet processed by heavy asymmetric rolling–annealing followed by light rolling–annealing [J]. Computational Materials Science, 2015, 100: 45−51.

[25] ZANCHETTA B D, DA. SILVA V K, SORDI V L, RUBERT J B, KLIAUGA A M. Effect of asymmetric rolling under high friction coefficient on recrystallization texture and plastic anisotropy of AA1050 alloy [J]. Transactions of Nonferrous Metals Society of China, 2019, 29(11): 2262−2272.

[26] TAMIMI S, CORREIA J P, LOPES A B, AHZI S, BARLAT F, GRACIO J J. Asymmetric rolling of thin AA-5182 sheets: Modelling and experiments [J]. Materials Science and Engineering: A, 2014, 603: 150−159.

[27] KAZEMI N A, JAMAATI R, AVAL H J. Asymmetric cold rolling of AA7075 alloy: The evolution of microstructure, crystallographic texture, and mechanical properties [J]. Materials Science and Engineering: A, 2021, 824: 141801.

[28] ENGLER O, KNARBAKK K. Temper rolling to control texture and earring in aluminium alloy AA 5050A [J]. Journal of Materials Processing Technology, 2021, 288: 116910.

[29] MA Zi-yao, ZHAN Li-hua, LIU Chun-hui, XU Ling-zhi, XU Yong-qian, MA Pei-pei, LI Jian-jun. Stress-level-dependency and bimodal precipitation behaviors during creep ageing of

Al−Cu alloy: Experiments and modeling [J]. International Journal of Plasticity, 2018, 110: 183−201.

[30] HO K C, LIN J, DEAN T A. Constitutive modelling of primary creep for age forming an aluminium alloy [J]. Journal of Materials Processing Technology, 2004, 153: 122−127.

[31] LI Gao-jie, GUO Ming-xing, DU Jin-qing, ZHUANG Lin-zhong. Synergistic improvement in bake-hardening response and natural aging stability of Al−Mg−Si−Cu−Zn alloys via non-isothermal pre-aging treatment [J]. Materials & Design, 2022, 218: 110714.

[32] LIU H, BELLÓN B, LLORCA J. Multiscale modelling of the morphology and spatial distribution of θ' precipitates in Al−Cu alloys [J]. Acta Materialia, 2017, 132: 611−626.

[33] SIMAR A, BRÉCHET Y, DE MEESTER B, DENQUIN A, PARDOEN T. Sequential modeling of local precipitation, strength and strain hardening in friction stir welds of an aluminum alloy 6005A-T6 [J]. Acta Materialia, 2007, 55(18): 6133−6143.

[34] ZHANG Jin, LI Zhi-de, XU Fu-shun, HUANG Cheng. Regulating effect of pre-stretching degree on the creep aging process of Al−Cu−Li alloy [J]. Materials Science and Engineering: A, 2019, 763: 138157.

[35] TAKAYAMA Y, FURUSHIRO N, KIMIJIMA E, KATO H. Change in crystallographic orientation distribution during superplastic deformation in an Al−Zn−Mg−Cu alloy [J]. Materials Science and Engineering: A, 2005, 410: 114−119.

[36] DONG Hai-peng, GUO Fei, HUANG Wei-jiu, YANG Xu-sheng, ZHU Xiang-hui, LI Hu, JIANG Lu-yao. Shear banding behavior of AA2099 Al−Li alloy in asymmetrical rolling and its effect on recrystallization in subsequent annealing [J]. Materials Characterization, 2021, 177: 111155.

[37] ZHAO Jiu-hui, DENG Yun-lai, ZHANG Jin, TANG Jian-guo. Effect of forging speed on the formability, microstructure and mechanical properties of isothermal precision forged of Al−Zn−Mg−Cu alloy [J]. Materials Science and Engineering: A, 2019, 767: 138366.

[38] STARINK M J, WANG S C. A model for the yield strength of overaged Al−Zn−Mg−Cu alloys [J]. Acta Materialia, 2003, 51(17): 5131−5150.

[39] BIGNON M, MA Z Y, ROBSON J D, SHANTHRAJ P. Interactions between plastic deformation and precipitation in Aluminium alloys: A crystal plasticity model [J]. Acta Materialia, 2023, 247: 118735.

[40] BARDEL D, PEREZ M, NELIAS D, DESCHAMPS A, HUTCHINSON C R, MAISONNETTE D, CHAISE T, GARNIER J, BOURLIER F. Coupled precipitation and yield strength modelling for non-isothermal treatments of a 6061 aluminium alloy [J]. Acta Materialia, 2014, 62: 129−140.

[41] RODGERS B I, PRANGNELL P B. Quantification of the influence of increased pre-stretching on microstructure−strength relationships in the Al−Cu−Li alloy AA2195 [J]. Acta Materialia, 2016, 108: 55−67.

[42] JIANG Mao-yuan, FAN Zheng-xuan, KRUCH S, DEVINCRE B. Grain size effect of FCC polycrystal: A new CPFEM approach based on surface geometrically necessary dislocations [J]. International Journal of Plasticity, 2022, 150: 103181.

[43] NIE Jian-feng. Precipitation and hardening in magnesium alloys [J]. Metallurgical and Materials Transactions A, 2012, 43: 3891−3939.

[44] AHMADI M R, POVODEN K E, ÖKSÜZ K I, FALAHATI A, KOZESCHNIK E. A model for precipitation strengthening in multi-particle systems [J]. Computational Materials Science, 2014, 91: 173−186.

[45] MURRAY J L. The aluminium−copper system [J]. International Metals Reviews, 1985, 30(1): 211−234.

[46] BELLÓN B, HAOUALA S, LLORCA J. An analysis of the influence of the precipitate type on the mechanical behavior of Al−Cu alloys by means of micropillar compression tests [J]. Acta Materialia, 2020, 194: 207−223.

[47] MIYOSHI H S, KIMIZUKA H J, ISHII A, OGATA S G. Temperature-dependent nucleation kinetics of Guinier−Preston zones in Al−Cu alloys: An atomistic kinetic Monte Carlo and classical nucleation theory approach [J]. Acta Materialia, 2019, 179: 262−272.

[48] SHIGEYASU K K M, TAKAHASHI S. Direct observaion for the interaction of dislocations with θ' precipitates in an aluminum−3.8wt.% copper alloy [J]. Journal of the Institute of Metals, 2021, 205: 116577.

[49] KAIRA C S, DE ANDRADE V, SINGH S S, KANTZOS C, KIRUBANANDHAM A, DE CARLO F, CHAWLA N. Probing novel microstructural evolution mechanisms in aluminum alloys using 4D nanoscale characterization [J]. Advanced Materials, 2017, 29(41): 1703482.

[50] RAKHMONOV J U, MILLIGAN B, BAHL S, MA D, SHYAM A, DUNAND D C. Progression of creep deformation from grain boundaries to grain interior in Al−Cu−Mn−Zr alloys [J]. Acta Materialia, 2023, 250: 118886.

[51] RAKHMONOV J U, BAHL S, SHYAM A, DUNAND D C. Cavitation-resistant intergranular precipitates enhance creep performance of θ'-strengthened Al−Cu based alloys [J]. Acta Materialia, 2022, 228: 117788.

[52] MILLIGAN B, MA D, ALLARD L, CLARKE A, SHYAM A. Crystallographic orientation-dependent strain hardening in a precipitation-strengthened Al−Cu alloy [J]. Acta Materialia, 2021, 205: 116577.

[53] BARLAT F, GLAZOV M V, BREM J C, LEGE D J. A simple model for dislocation behavior, strain and strain rate hardening evolution in deforming aluminum alloys [J]. International Journal of Plasticity, 2002, 18(7): 919−939.

[54] DAHLGREN S D. Coherency stresses, composition and dislocation interactions for θ'' precipitates in age-hardened Al−Cu [J]. Metallurgical Transactions A, 1976, 7: 1401−1405.

[55] HOSFORD W F, ZEISLOFT R H. The anisotropy of age-hardened Al−4PctCu single crystals during plane-strain compression [J]. Metallurgical and Materials Transactions B, 1972, 3: 113−121.

[56] MISHRA S, YADAVA M, KULKARNI K N, GURAO N P. A theoretical investigation of the effect of precipitate habit plane on plastic anisotropy in age hardenable aluminium alloys [J]. Modelling and Simulation in Materials Science and Engineering, 2018, 26(5): 055011.

利用异步轧制提高 AA2219 合金的蠕变时效成形能力

曾泉清[1]，王东耀[2]，马博林[1,3]，徐永谦[1,3]，
黄明辉[1,2]，唐 磊[4]，刘长志[5]，鄢东洋[5]，湛利华[1,2,3]，杨有良[1,3]

1. 中南大学 轻合金研究院，长沙 410083；
2. 中南大学 机电工程学院，长沙 410083；
3. 中南大学 极端服役性能精准制造全国重点实验室，长沙 410083；
4. 中南大学 材料科学与工程学院，长沙 410083；
5. 北京航宇系统工程研究所，北京 100076

摘 要：通过蠕变变形实验、拉伸试验、电子背散射衍射(EBSD)和透射电子显微镜(TEM)探讨了非对称轧制(ASR)和冷轧(CR)对 AA2219 合金蠕变时效行为的影响。实验结果显示，在蠕变应力为 $1.2\sigma_{0.2}$($\sigma_{0.2}$ 为屈服强度)的条件下，ASR 试样的蠕变应变比 CR 试样的高 50%。当蠕变应力为 $0.5\sigma_{0.2}$ 时，ASR 试样表现出更优的力学性能，其抗拉强度达到 525 MPa，屈服强度达到 338 MPa，伸长率达到 15.2%。上述实验结果是因为 ASR 工艺有效地细化了晶粒尺寸并促进了晶粒的再结晶。相较于 CR 工艺，ASR 工艺能使 AA2219 合金形成更高立方体织构和位错密度的组织。此外，与 CR 试样相比，ASR 试样的 θ'析出相呈更加弥散、细小分布，同时具有较大的平均泰勒系数。

关键词：AA2219 合金；异步轧制；蠕变时效行为；织构；析出相；力学性能

(Edited by Wei-ping CHEN)